

1 **MethylationToActivity: a deep-learning framework that reveals**
2 **promoter activity landscapes from DNA methylomes in individual**
3 **tumors**

4

5 Justin Williams¹, Beisi Xu², Daniel Putnam¹, Andrew Thrasher¹, Chunliang Li³, Jun
6 Yang⁴ and Xiang Chen¹

7

8 ¹Department of Computational Biology, St. Jude Children's Research Hospital, Memphis,
9 Tennessee, United States

10 ²Center for Applied Bioinformatics, St. Jude Children's Research Hospital, Memphis, Tennessee,
11 United States

12 ³Department of Tumor Cell Biology, St. Jude Children's Research Hospital, Memphis,
13 Tennessee, United States

14 ⁴Department of Surgery, St. Jude Children's Research Hospital, Memphis, Tennessee, United
15 States

16

17

18

19 Corresponding author: Xiang Chen
20 Department of Computational Biology

21 St. Jude Children's Research Hospital

22 262 Danny Thomas Place

23 Mail Stop 1135

24 Memphis, TN 38105

25 U.S.A.

26 Tel: +1 901 595 7074

27 Fax: +1 901 595 7100

28 Email: xiang.chen@stjude.org

29

30 **Abstract**

31 Although genome-wide DNA methylomes have demonstrated their clinical value as reliable
32 biomarkers for tumor detection, subtyping, and classification, their direct biological impacts at
33 the individual gene level remain elusive. Here we present MethylationToActivity (M2A), a
34 machine learning framework that uses convolutional neural networks to infer promoter activities
35 (H3K4me3 and H3K27ac enrichment) from DNA methylation patterns for individual genes.
36 Using publicly available datasets in real-world test scenarios, we demonstrate that M2A is highly
37 accurate and robust in revealing promoter activity landscapes in various pediatric and adult
38 cancers, including both solid and hematologic malignant neoplasms.

39 **Keywords:**

40 DNA methylation, histone modifications, convolutional neural network, transfer learning

41

42 **Background**

43 Transcriptional regulation is fundamental to the identity and function of cells. Deregulation of
44 gene expression is a defining feature of common diseases, including cancers. Promoters, the
45 regulatory regions surrounding the transcription starting sites (TSSs), integrate signals from
46 distal enhancers and local histone modifications (HMs) to initiate transcription. Almost half of
47 human protein-coding genes harbor multiple TSSs; consequently, promoter activities determine
48 both the level of transcription and the transcript isoforms that are expressed, with the latter
49 potentially having different translation efficiencies and encoding different protein sequences [1].
50 Tumors frequently use alternative promoters to increase the isoform diversity [2, 3], to activate
51 oncogenes that are normally repressed [1-3], and to evade host immune attacks by
52 immunoediting [3, 4]. Compared to cancers in adults, pediatric tumors harbor fewer mutations [5,
53 6] and use epigenetic deregulation to promote tumorigenesis and progression [7].

54 Promoter activities can be determined experimentally through transcriptomic approaches,
55 such as CAP analysis gene expression (CAGE), or through epigenomic approaches, including
56 chromatin immunoprecipitation followed by sequencing (ChIP-seq) [8]. Because of transcript
57 degradation by 5' RNA exonucleases, ChIP-seq approaches for specific HMs have been the
58 gold standard for studying promoter activities [9]. Several studies [10-12] have demonstrated
59 that HMs and other epigenetic features can be used to predict gene expression. Using a linear
60 regression model, Karlić et al. show that approximately 50%–60% of the variation in gene
61 expression can be accounted for, and that ~50% of the variation in gene expression can be
62 modeled by promoter H3K27ac enrichment alone [10]. Subsequent work by Dong et al. further
63 explained 69% of gene expression variance using a hybrid random forest/linear regression
64 model with features derived from 11 HMs, one histone variant, and DNase I hypersensitivity
65 [11]. More recently, Singh et al. used deep-learning models on five HMs to predict gene
66 expression status (high/low) and achieved an average AUC of 0.80 [12]. However, the scarcity
67 of pediatric tumors, the limited amounts of fresh starting material available, and the

68 extensive workload involved in acquiring the promoter activity landscapes constrain their
69 interrogation for individual patient tumors [13, 14].

70 DNA methylation (DNAm) is a well-studied, relatively stable, and inheritable epigenetic
71 regulatory mechanism that involves transferring a methyl group to cytosine (C) to form 5-
72 methylcytosine (5mC), mostly in the CpG context. In contrast to HMs, DNAm can be accurately
73 and robustly profiled in various tissues, including archival formalin-fixed, paraffin-embedded
74 (FFPE) tumor samples, through both array [15, 16] and sequencing [17] platforms; therefore, it
75 has exceptional applicability to studying epigenetic deregulation in tumors. Consequently,
76 genome-wide DNAm profiles represent a widely available epigenetic asset for studying
77 epigenetic abnormalities in primary tumors.

78 The DNAm pattern is mechanistically connected with transcription factor binding and HMs
79 [18-25]. It also plays critical roles in establishing the chromatin structure in physiologic and
80 pathologic conditions [26, 27]. Moreover, recent applications of machine learning to genome-
81 wide DNAm patterns have demonstrated that DNAm can accurately predict the patterns of
82 chromatin packaging (A/B compartments, the square of the Pearson correlation coefficient $R^2 =$
83 0.50–0.66) [28-30] and can reveal distinct subgroups with prognostic significance among
84 patients with cancer [31, 32]. Recently, DNAm signature–based molecular classifiers were
85 shown to improve diagnostic accuracy, as compared to that of traditional schemes, further
86 demonstrating the critical regulatory roles of DNAm in tumor development [33, 34]. However,
87 unlike HMs, where established biological interpretations of various marks have resulted in a
88 general “histone code” hypothesis [35, 36], the relation between DNAm signatures and their
89 transcriptional regulatory roles is complex and nonlinear. In many cases, even promoter DNAm
90 may positively and negatively correlate with gene expression depending on the genomic
91 structure involved in a given tumor [37]. Consequently, with few exceptions (e.g.,
92 hypermethylation of the promoters of *RB1*, *CDKN2A*, and *MGMT*) [38], the contribution of

93 DNAm to the regulation of expression of individual genes remains largely elusive [39-41].
94 Recent attempts to use DNAm signatures to account for gene expression levels have had
95 limited success, with the best model (binomial distribution probit regression [BPR] model)
96 capturing 25%–49% of the expression variations [42]. Undoubtedly, the lack of interpretability
97 of the DNAm pattern at the individual gene level has severely hampered our understanding of
98 the biological significance of DNAm signatures.

99 To address these challenges, we have developed MethylationToActivity (M2A), a deep-
100 learning framework. The central hypothesis of M2A is that the complex relation between DNAm
101 signatures and promoter activities (measured as H3K4me3 and H3K27ac enrichment in the
102 TSS \pm 1 kb region) can be captured by incorporating both summary statistics extracted from
103 window-based CpG methylation levels and high-order spatial information from these windows in
104 the promoter and flanking regions (up to 25 kb from the TSS). Using a cohort of six pediatric
105 neuroblastoma (NBL) orthoptic patient-derived xenograft (O-PDX) samples profiled in the
106 Pediatric Cancer Genome Project (PCGP) [43], we trained the model using whole-genome
107 bisulfite sequencing (WGBS) data to predict the enrichment of H3K4me3 and H3K27ac (two
108 HMs critical for promoter [10]) for genome-wide annotated promoters. We validated the
109 predictive accuracy of the model in the remaining NBL samples ($N=10$, WGBS) from the
110 same cohort. We further confirmed its accuracy and generalizability in diverse tumor types from
111 four publicly available datasets representing real-world applications, including (1) pediatric
112 rhabdomyosarcoma (RMS) O-PDX tumors profiled in the Pediatric Cancer Genome Project
113 ($N=16$, WGBS) [44]; (2) a set of commonly used cell lines profiled in ENCODE ($N=9$,
114 WGBS) [45]; (3) primary acute myeloid leukemias (AMLS) profiled by the BLUEPRINT
115 consortium ($N=19$, WGBS) [46]; and (4) a large primary Ewing sarcoma (EWS) cohort using
116 reduced representation bisulfite sequencing (RRBS) ($N=140$) [22]. These
117 applications demonstrate that M2A can accurately reveal promoter activities from DNAm

118 patterns, which will be of great use not only in functionally interpreting differential DNAm
119 patterns but also in profiling promoter usage in individual patient tumors. This will facilitate
120 precision medicine by tailoring treatments based on both genetic variants and epigenetic
121 deregulations.

122

123 **Results**

124 **Extensive diversity of promoter activity among *MYCN*-amplified NBL cell lines 125 and O-PDX models**

126 To date, most cancer HM profiling studies have made use of tumor models, including cell
127 lines, xenografts, and more recently, organoids. Technical limitations and challenges when
128 working with human tumor tissues prevent the generation of high-quality ChIP-seq profiles for
129 primary patient specimens [47]. Despite the documented epigenetic heterogeneity [48], a
130 common practice in deciphering major HM deregulations in various cancers is to extrapolate the
131 epigenetic profiles from related cancer models (surrogate models). Many studies [43, 44, 49-52]
132 have compared model systems to primary tumors with respect to characteristics such as
133 mutations, gene expression, and DNAm signatures. In this study, we began by evaluating the
134 level of promoter activity diversity in closely related NBL models. Specifically, we evaluated
135 promoter activity, as measured by the H3K27ac level, in three O-PDX models (SJNBL046,
136 SJNBL108, and SJNBL013763) and three cell line models (IMR-32, NB-5, and SKNBE2) that
137 harbor *MYCN* amplification with no other major oncogenic mutations. All samples displayed a
138 bimodal distribution of promoter H3K27ac levels across the genome (Additional file 1: Figure
139 S1), and O-PDX models had a marginally higher fraction of active promoters (mean: 31.9%,
140 range: 27.6%–36.1%) than did cell line models (mean: 26.1%, range: 25.6%–26.7%)
141 ($P = 0.14$, Student's *t*-test). However, there were extensive variations in the promoter

142 activities in both the cell line models (Figures 1a and 1d) and the O-PDX models (Figures 1b
143 and 1e). Moreover, greater divergence was observed between a cell line model and an O-PDX
144 model (mean: 34.9%, range: 29.9%–39.0%) than between two cell line models (mean: 31.0%,
145 range: 29.2%–32.1%; $P=0.44$, Student's *t*-test) or between two O-PDX models (mean:
146 31.0%, range: 22.9%–37.0%; $P=0.02$, Student's *t*-test) (Figure 1f). Variations in promoter
147 activity may play a significant role in the transcriptional deregulation of individual tumors, as a
148 substantial fraction of established cancer consensus genes (22.4% in O-PDX models and 31.1%
149 in cell line models, including *APOBEC3B*, *TGFBR2*, *PAX7*, *HOXA11*, *PDCD1LG2*, *PTK6*,
150 *BCL11B*, *FAS*, and *MYC*; (Additional file 2: Table S1) displayed heterogeneous promoter
151 activities in the surveyed tumor models. Therefore, we sought to develop a computational
152 approach to infer the promoter activity landscape for individual tumors.

153

154 **M2A: a deep-learning framework to reveal promoter activities from DNA
155 methylation**

156 DNA methylation plays a critical role in determining the framework of gene expression for a given
157 cell/cellular state. However, the highly complex and non-linear relations between DNA methylation
158 patterns and HMs severely hamper the interpretability of the biological impact of differential
159 DNA methylation patterns. Previous studies have shown the usefulness of extracting higher-order
160 methylation features [42], for predicting gene expression. Moreover, recent studies applied
161 deep-learning approaches to infer DNA methylation states from their local sequence composition and
162 adjacent DNA methylation states [53]. We hypothesize that these high-level DNA methylation features (that capture
163 the spatial information from DNA methylation patterns in the promoter and regions in its vicinity) could also
164 provide an opportunity to infer promoter activities such as H3K27ac and H3K4me3 enrichment
165 accurately. We propose to use a convolutional neural network (CNN)-based deep-learning
166 framework to extract such features.

167 The M2A conceptual framework and workflow is shown in Figure 2. M2A starts with raw
168 DNAm feature extraction from around individual TSSs (Figure 2a). This is followed by high-level
169 feature extraction through the CNN layers and mapping between the generalized feature and
170 the final output (i.e., the H3K4me3 and H3K27ac of the promoter) in the fully connected (FC)
171 layers. The vanilla model described in this report was trained on six NBL PDX tumors
172 (SJNBL046_X, SJNBL013761_X1, SJNBL012401_X1, SJNBL013762_X1, SJNBL013763_X1,
173 and SJNBL015724_X1; Figure 2b) for which comprehensive genomic and epigenomic profiling
174 data are available, including the results of whole-genome sequencing, whole-exome sequencing,
175 RNA sequencing, WGBS, and ChIP-seq of eight histone marks (H3K4me1, H3K4me2,
176 H3K4me3, H3K27me3, H3K27ac, H3K36me3, H3K9/14ac, and H3K9me3), CTCF, BRD4, and
177 RNA polymerase II (PolII).

178 We started with an analysis of the information content in DNAm patterns by examining the input
179 feature distribution in different windows, among active (high H3K27ac), poised (high H3K4me3
180 and low H3K27ac), and inactive promoters (low H3K4me3 and low H3K27ac) in the six NBL O-
181 PDX training samples. These features show distinct patterns among the three promoter
182 categories (Additional File 1: Figure S2), indicating the feasibility of modeling promoter activities
183 from DNAm patterns. Although the interpretability of CNN extracted features remains an active
184 field of research in deep-learning [54], we examined the efficacy of CNN extracted features in
185 modeling the promoter activities. We first compared the square of Pearson's correlation (R^2)
186 between each feature (both raw input and CNN extracted features) and the response variable
187 (H3K27ac) in the training set, The analysis revealed that CNN-extracted features have
188 significantly higher R^2 with the response (250 bp: $P = 1.5 \times 10^{-11}$, 2500 bp $P = 3.9 \times 10^{-5}$,
189 Wilcoxon signed-rank test, Additional File 1: Figure S3). We further evaluated the best features
190 for both raw input and CNN-extracted features in the validation samples and again the CNN-

191 extracted features significantly outperformed the raw input features (250 bp: $P = 1.1 \times 10^{-5}$,
192 2500 bp $P = 1.1 \times 10^{-5}$, Wilcoxon signed-rank test, Additional File 1: Figure S3).

193 **M2A produces a highly accurate landscape of promoter activity in pediatric NBL**

194 To evaluate the performance of M2A, we first explored its performance in the remaining NBL
195 samples in the cohort (the validation set), including one O-PDX tumor, one primary autopsy
196 tumor, and eight cell lines. Using the validation set, we compared the performance of the M2A
197 framework of three CNN layers and two FC layers (Figure 2) with three frequently used
198 statistical and machine learning approaches (baseline models), namely multivariate adaptive
199 regression splines (MARS), random forest, and artificial neural network (ANN) consisting of only
200 two FC layers. In every instance, the M2A framework outperformed baseline models (Additional
201 file 2: Table S2). From a qualitative perspective, M2A correctly revealed the bimodal distribution
202 of the promoter activities for both H3K4me3 and H3K27ac in all samples, and from a
203 quantitative perspective, the inferred genome-wide promoter activity landscape was
204 highly accurate for individual samples for both H3K4me3 ($R^2 = 0.933 \pm 0.019$; RMSE =
205 0.621 ± 0.072) (Figures 3a and 3d) and H3K27ac ($R^2 = 0.799 \pm 0.053$; RMSE =
206 0.644 ± 0.074) (Figures 3b, and 3c). Moreover, the addition of CNN layers was merited, as
207 there was a decrease in the prediction error (measured as $1 - R^2$) from the next highest
208 performer by 17.8% ($P = 0.0020$, Wilcoxon signed-rank test) and 12.4% ($P = 0.0020$,
209 Wilcoxon signed-rank test) for the model topologies for H3K4me3 and H3K27ac, respectively
210 (Additional file 2: Table S2).

211 Our analysis of MYCN-amplified NBL cell line and O-PDX models has revealed substantial
212 variations in their promoter activities, which is a potential caveat to the practice of surrogate
213 model (representing primary tumor epigenomes by a few profiled models). Conversely,
214 M2A produced highly accurate promoter activity landscapes, significantly outperforming the
215 observed consistency between training and testing samples for both H3K4me3 ($R^2 =$

216 0.891 ± 0.023 , $P = 2.3 \times 10^{-5}$, Wilcoxon rank-sum test) and H3K27ac ($R^2 =$
217 0.720 ± 0.045 , $P = 9.5 \times 10^{-5}$, Wilcoxon rank-sum test; Additional file 2: Table S3).
218 Remarkably, in nine (of 10) test samples, the accuracy of the M2A-inferred promoter H3K27ac
219 activity was better than the highest similarity attained by any individual training sample
220 ($P = 0.027$, Wilcoxon signed-rank test). The same pattern was observed for H3K4me3 levels,
221 with M2A being more accurate for nine of 10 samples ($P = 0.037$, Wilcoxon signed-rank test),
222 demonstrating the accuracy of M2A in revealing individual tumor promoter activity landscapes.
223 Finally, the predictive accuracy of M2A was comparable to the experimental consistency
224 observed between replicates from the same cell lines profiled in ENCODE for H3K4me3 (R^2
225 $= 0.933 \pm 0.018$ for M2A vs. 0.922 ± 0.056 for ENCODE replicates [$N = 25$]; $P = 0.55$,
226 Wilcoxon rank-sum test) (Figure 3a; Additional file 2: Table S4). The accuracy of M2A also
227 approached the replicate consistency for H3K27ac ($R^2 = 0.799 \pm 0.050$ for M2A vs.
228 0.849 ± 0.047 for ENCODE replicates [$N = 26$]; $P = 0.0078$, Wilcoxon rank-sum test)
229 (Figure 3b; Additional file 2: Table S4). Measurement of the root mean square error (RMSE)
230 revealed a similar pattern (Additional file 2: Table S4).

231

232 **M2A is generalizable and scalable**

233 Aside from the model accuracy, there are two additional requirements with practical importance
234 for deploying a machine learning model (such as M2A) in real-world applications: (1)
235 generalizability, i.e., M2A needs to achieve a similar performance with a set of unseen test
236 samples, including tumor/tissue types not used in the model training; and (2)
237 scalability, i.e., M2A must be able to be applied efficiently to external data.

238 We first demonstrated the accuracy, generalizability, and scalability of M2A by
239 using test samples from rhabdomyosarcoma (RMS) O-PDX tumors. The RMS O-PDX dataset

240 consists of 16 pediatric RMS tumors (11 embryonal, four alveolar, and one spindle subtype,
241 termed ERMS, ARMS, and spindle subtypes, respectively). As with the NBL cohort, each RMS
242 sample was extensively profiled, including by WGBS, RNA-seq, and ChIP-seq of H3K4me3 and
243 H3K27ac. Using the vanilla M2A model (the 3CNN-FC model trained on the six NBL PDX
244 samples), M2A achieved an overall predictive accuracy with the RMS dataset that was
245 comparable to that of the NBL test group for both H3K4me3 ($R^2 = 0.937 \pm 0.017$, $P = 0.30$;
246 RMSE = 0.639 ± 0.119 , $P = 0.82$, Wilcoxon rank-sum test) (Figures 3a and 3f; Additional file 2:
247 Table S5) and H3K27ac ($R^2 = 0.790 \pm 0.037$, $P = 0.44$; RMSE = 0.589 ± 0.084 , $P = 0.058$,
248 Wilcoxon rank-sum test) (Figures 3b and 3e; Additional file 2: Table S5), which was comparable
249 to or significantly outperformed the observed similarities between two different RMS tumors for
250 H3K4me3 ($R^2 = 0.917 \pm 0.028$, $P = 0.0020$; RMSE = 0.646 ± 0.133 , $P = 0.64$, Wilcoxon
251 rank-sum test) and H3K27ac ($R^2 = 0.780 \pm 0.066$, $P = 0.43$; RMSE = 0.550 ± 0.095 , $P =$
252 0.14 , Wilcoxon rank-sum test). The accuracy of the inferred H3K4me3 activity was comparable
253 to the inter-replicate consistency of the ENCODE samples ($P = 0.83$, Wilcoxon rank-sum test).

254 By definition, generalizability can be achieved only in the absence of over-fitting (or
255 “memorization” of the training data). Neural networks often fall victim to this problem through a
256 combination of factors, including relatively small training datasets and/or over-parameterization.
257 The relatively consistent expression of housekeeping genes across different tissues may lead to
258 an inaccurate (often inflated) interpretation of the performance measurement in such a model,
259 as evidenced by the relatively high R^2 value (0.663 ± 0.040) between the promoter H3K27ac
260 level of a random RMS test tumor and the most similar NBL training tumor (Additional file 1:
261 Figure S4a). Therefore, we focused on the set of genes that are differentially expressed (DE) in
262 RMS and NBL PDX samples [51], for which an over-fitted or memorized model would perform
263 poorly. Not surprisingly, the average correlative consistency between the NBL validation
264 samples and the most similar NBL training sample dropped from 0.755 to 0.599 when the

265 measurement was restricted to promoters encoding the DE genes (Additional file 1: Figure S4b),
266 whereas a sharp decline (from 0.663 to 0.259) was also observed for RMS test tumors
267 (Additional file 1: Figure S4b). Conversely, the six-PDX NBL-trained M2A model maintained
268 high accuracy for promoters of DE genes in both the NBL validation set ($R^2 = 0.729 \pm 0.071$
269 and the RMS test set ($R^2 = 0.715 \pm 0.044$) (Additional file 1: Figure S4b), further
270 demonstrating the generalizability of M2A.

271 M2A is efficient and scalable. For a local implementation of M2A (source code, built models
272 and a Docker image available at <https://github.com/chenlab-sj/M2A>), the training of the vanilla
273 M2A model (with six NBL O-PDX tumors) takes approximately 16 min (using a Tesla P100-
274 16GB GPU). The feature extraction and promoter activity prediction from WGBS data (as a
275 genome-wide DNAm level file in a tab-delimited text format) can be executed on a personal
276 computer (in this case, we used a MacBook Air with a 2.2-GHz Intel Core i7 and 8-GB 1600-
277 MHz DDR3 RAM) and takes 15–19 min. Moreover, we have implemented a cloud version of
278 M2A (<https://platform.stjude.cloud/workflows/methylation-to-activity>), available to the general
279 research community.

280

281 **Transfer learning further improves the performance of M2A with minimal
282 additional input in the target domain.**

283 Although we have demonstrated the generalizability of M2A in the RMS dataset, the fact that
284 epigenetic genes are frequently mutated in pediatric tumors [7] raises the possibility that
285 individual tumor types carry a type-specific interpretation of the DNAm patterns. When ChIP-seq
286 measurement is available for sufficient samples, a type-specific model is desirable. However,
287 although pediatric solid tumors as a group constitute a rare disease, they comprise many
288 different tumor types, and it is rare to have sufficiently profiled samples available for many of

289 them. In addressing this challenge, we hypothesize that a fixed feature-extraction strategy
290 (transfer learning) can achieve the goal of deriving an efficient tumor type–specific model by
291 using a small labeled dataset. A primary assumption here is that generalized features extracted
292 based on a large dataset are similarly informative for apparently different tasks. The feature
293 learning and selection characteristics of CNNs provide exceptional portability in various tasks
294 with extremely small labeled datasets.

295 In M2A, the CNN layers capture generalized DNAm features and the FC layers learn the
296 mapping function between the DNAm features and the promoter activities. Here we start with
297 the pretrained vanilla M2A model, fix the feature-extraction layers (CNN layers), and use a
298 single sample from the target tumor type to update the mapping function (the weights and
299 biases of the FC layers). Because the consistency of M2A for H3K4me3 approached the inter-
300 replicate consistency in both NBL and RMS datasets, we focused on H3K27ac inference for
301 transfer learning. Upon performing transfer learning with a single sample in the RMS dataset,
302 we observed significantly improved accuracy ($R^2 = 0.813 \pm 0.038$, $P = 3.1 \times 10^{-5}$,
303 Wilcoxon signed-rank test) (Figures 3b, 3g, and 3h; Additional file 2: Table S5). Moreover, this
304 model significantly outperformed a single RMS sample model with the identical model
305 architecture, in which both the CNN layer and the FC layers were derived from the RMS training
306 sample ($P = 9.2 \times 10^{-5}$, Wilcoxon signed-rank test) (Additional file 1: Figure S5; Additional
307 file 2: Table S6) and marginally outperformed the observed similarities between different RMS
308 tumors ($P = 0.053$, Wilcoxon rank-sum test). This analysis demonstrated the value of both the
309 pretrained CNN layers for general feature extraction and a single profiled sample in the target
310 domain. Consequently, we applied transfer learning to both the EWS and AML datasets.
311 However, transfer was not feasible in the ENCODE dataset because those cell lines were
312 derived from different tissues.

313

314 **M2A accurately reveals promoter activity landscapes in adult tumors and in**
315 **hematologic malignant neoplasms**

316 We next evaluated the performance of M2A in independently collected datasets, including ones
317 for adult tumors and hematologic malignant neoplasms. Upon analyzing nine ENCODE cell
318 lines, we found that differences in antibody usage and experimental protocols between the
319 ENCODE and NBL datasets resulted in different signal-to-noise profiles (Additional file 1: Figure
320 S6), with higher RMSE values between the model predictions and the actual observations
321 (H3K4me3: 0.961 ± 0.238 , $P = 0.0019$; H3K27ac: 0.918 ± 0.188 , $P = 2.6 \times 10^{-4}$,
322 Wilcoxon rank-sum test). However, the predicted activities remained highly correlated with the
323 experimental measurements (H3K4me3: $R^2 = 0.895 \pm 0.027$; H3K27ac: $R^2 = 0.680 \pm 0.149$)
324 (Additional file 1: Figure S7). Although the accuracy of H3K4me3 was relatively uniform, H1-
325 ESC and SK-N-SH were outliers with a substantially lower accuracy of H3K27ac inference (by
326 the boxplot-based method [55]) (Additional file 2: Table S4; Additional file 1; Figure S8a). An
327 investigation of the promoter activity (the measured and inferred H3K27ac levels) and the
328 measured gene expression in H1-ESC revealed that a subset of actively transcribed genes
329 showed little or no H3K27ac levels in their promoters, where M2A inferred relatively strong
330 promoter activity (Additional file 1: Figure S8b). Consequently, the inference of promoter activity
331 by M2A outperformed the actual measurement in terms of both the quantitative consistency with
332 the gene expression level ($R^2 = 0.536$ for the M2A-inferred H3K27ac level vs. 0.435 for the
333 measured H3K27ac level) (Additional file 1: Figures S8b and S8c) and the accuracy in predicting
334 expressed genes (AUC = 0.891 for the M2A-inferred H3K27ac level and 0.881 for observed
335 H3K27ac level) (Additional file 1: Figure S9d). We also observed a small fraction of inferred
336 active promoters without strong expression; these may represent genes subject to
337 transcriptional pausing (where transcription is initiated but there is no elongation), a distinctive

338 feature of undifferentiated stem cells [56]. Similarly, better consistency with gene expression
339 levels was observed in SK-N-SH (Additional file 2: Table S7).

340 We further evaluated the performance of M2A in revealing promoter activities in 19 acute
341 myeloid leukemia (AML) primary patient samples collected by the BLUEPRINT consortium,
342 which is part of the International Human Epigenome Consortium (IHEC) [46]. Analyses of
343 observed promoter activity (measured by H3K27ac level) and gene expression (measured in
344 fragments per kilobase of transcript per million mapped reads [FPKM]) in the same sample
345 revealed non-uniform qualities with a wide range of consistency (mean $R^2 = 0.539$, range:
346 0.178–0.720) (Additional file 2: Table S8). Similarly, the M2A-inferred promoter activity
347 landscape displayed substantial variability with respect to the observed activities among these
348 samples (mean $R^2 = 0.473$, range: 0.031–0.729). Strikingly, the consistency between the
349 observed promoter activity and gene expression was highly predictive of the performance of
350 M2A with individual samples ($R^2 = 0.975$, $P = 4.1 \times 10^{-15}$, Pearson's correlation test)
351 (Additional file 1: Figure S10). Finally, although gene expression was not used in model
352 generation with M2A (for the vanilla model or the transfer learning step), the promoter activity
353 inferred by M2A showed uniform consistency with gene expression (mean $R^2 = 0.628$, range:
354 0.541–0.684) (Additional file 2: Table S8). These results jointly suggest that the ChIP-seq library
355 quality is a potential confounding factor for both the consistency between the observed (from
356 ChIP-seq) and the M2A-inferred promoter activity landscapes and the consistency between the
357 observed promoter activity and gene expression in these samples.

358

359 **Promoter activity landscape inferred by M2A faithfully recapitulates the subtype
360 difference between embryonal and alveolar rhabdomyosarcomas**

361 Identifying recurrent epigenetic deregulations (epi-drivers) is a primary research focus in cancer
362 epigenome studies [57]. To this end, we investigated whether subtype-specific epigenetic
363 deregulation was captured in M2A-revealed promoter landscapes in the RMS O-PDX tumors. A
364 t-SNE embedding using M2A-inferred promoter activity landscapes (from the NBL-trained model)
365 recapitulated the clear separation of ARMS and ERMS tumors (Figure 4a) in the DNAm profiles
366 (data not shown), which further demonstrates the generalizability of the CNN-extracted high-
367 order DNAm features. Importantly, when focusing on the promoters of DE genes in the ARMS
368 and ERMS subtypes, the vanilla M2A model faithfully retained the subtype-specific promoter
369 activity patterns ($R^2 = 0.713$ for DE genes with a single annotated promoter; 0.621 when all
370 annotated promoters for DE genes were included) (Additional file 1: Figures S11a and S11c).
371 Transfer learning using data from a single RMS further improved the consistency ($R^2 = 0.758$
372 and 0.673, respectively) (Additional file 1: Figures S11b and S11d).

373 *GAS2* is a gene selectively expressed in ERMS [44]. Although promoter hypomethylation
374 was found in the ARMS tumors, the M2A model correctly predicted significantly stronger
375 promoter activities in ERMS tumors ($P = 0.01$, Wilcoxon rank-sum test) (Figures 4b and 4d).
376 Similarly, although both ERMS and ARMS tumors had *NOS1-005* promoter hypomethylation,
377 strong promoter activity was predicted in ARMS tumors only ($P = 0.0015$, Wilcoxon rank-sum
378 test) (Figures 4c and 4e), consistent with the ChIP-seq measurement.

379

380 **M2A reveals the contribution of differentially methylated regions to promoter
381 activities**

382 Although DNA methylation patterns, including differentially methylated regions (DMRs), are well-
383 established biomarkers for diverse diseases and have revealed molecularly and clinically
384 different subtypes for many cancers, their functional importance in individual gene regulation is
385 less clear [39-41]. For example, many cancer-specific CpG island hypermethylation regions

386 occur in genes that normally are not expressed or are expressed at only a low level [58].
387 Moreover, even in genes that are both differentially expressed and differentially methylated in
388 different subtypes, up-regulated samples can be associated with hypomethylation,
389 hypermethylation, or both [37, 44]. The observed nonlinear relation between DNA methylation
390 and gene expression complicated the functional interpretation of specific DMRs. In this analysis,
391 we interpret the functional roles of DMRs based on the promoter activities of their associated
392 DE genes.

393 To summarize unambiguously the contribution of DMRs to differential promoter activities, we
394 focused on 371 genes in ERMS and ARMS that have a single annotated promoter and that are
395 both differentially expressed (197 are over-expressed in ERMS, 172 are over-expressed in
396 ARMS) and differentially methylated (169 are hypomethylated, 128 are hypermethylated, and 74
397 have both hypomethylation and hypermethylation) in the two major RMS subtypes (Additional
398 file 2: Tables S9 and S10) [44]. Among these genes, 140 promoters showed significantly higher
399 H3K27ac measurements in the over-expressed subtype (FDR < 0.1, Wilcoxon rank-sum test),
400 whereas 206 promoters had measurements that were significantly higher when the DNAm-
401 based H3K27ac activity was measured. These 206 promoters included 118 of the 140
402 promoters identified using the observed signals. These results suggest that M2A can reveal the
403 role of DMRs in modulating the promoter activities of affected genes in a context-specific
404 manner.

405

406 **M2A identifies subtype-specific promoter usage encoding different protein
407 isoforms in rhabdomyosarcoma**

408 Alternative promoter usage is an important pretranslational mechanism for tissue-specific
409 regulation as it affects the diversity of isoforms available. Recently, light was shed on the

410 pervasiveness of alternative promoter usage in cancer; in some cases, promoter usage is a
411 more accurate reflection of patient survival than is gene expression [2]. Among 10,835 active
412 genes with multiple annotated promoters in the RMS dataset, we found 2,584 genes (24%) with
413 alternative primary promoter usage among 16 samples. We focused on 562 genes that 1) were
414 active in both the ERMS and ARMS subtypes and 2) had subtype-specific promoter usage. We
415 explored the accuracy of M2A in predicting alternative promoter usage in ARMS and ERMS
416 (Additional file 2: Table S11).

417 Based on measured promoter activities, 428 genes exhibited significant usage difference
418 between the two subtypes (FDR < 0.1, Wilcoxon rank-sum test [used as the ground truth]). The
419 M2A-inferred promoter activity landscape revealed 276 genes for which there was a significant
420 difference in promoter usage between the subtypes (FDR < 0.1, Wilcoxon rank-sum test), and
421 210 of them matched the ground truth (precision = 0.76, recall = 0.49, F1 score = 0.60)
422 (Additional file 2: Table S11).

423 PDZ Domain Containing Ring Finger 3 (*PDZRN3*) is a known target of the PAX3/7–FOXO1
424 fusion protein [59–61], which blocks terminal differentiation in myogenesis [62]. M2A predicted a
425 subtype-specific promoter usage pattern in *PDZRN3*. Functional studies have shown that
426 *PDZRN3* regulates myoblast differentiation into myotubes through transcriptional and
427 posttranslational regulation of Id2 [62]. Its over-expression in ARMS was primarily driven by the
428 fusion protein binding adjacent to an alternative promoter (*PDZRN3-006*) located 191 kbp
429 downstream of the canonical promoter (*PDZRN3-001*) (Figure 5a). The subtype-specific isoform
430 usage is accompanied by DMRs of the alternative promoter and its immediate downstream
431 regions and is further confirmed by RNA-seq read alignment (Figure 5a). Compared to the
432 canonical isoform expressed in ERMS, the ARMS-preferred *PDZRN3-006* isoform lacks the
433 RING-finger and Sina domains in the N-terminus and harbors a shorter PDZ domain. The
434 isoform difference, as well as the differences in expression level, between subtypes may

435 contribute to the impairment of myogenesis at different stages in the development of ARMS and
436 ERMS tumors.

437

438 **M2A identifies alternative promoter usages with potential prognostic values in**
439 **Ewing sarcoma**

440 We next examined the predicted epigenetic promoter activities in 140 EWS samples with DNAm
441 data assayed by RRBS [22]. Three of these samples had matching ChIP-seq profiles for
442 H3K4me3 and H3K27ac. To interrogate this dataset, we applied the pretrained vanilla model
443 with transfer learning, as detailed above, to recalibrate the weights mapping the high-level
444 features to the promoter activities in the EWS cohort. Despite the difference in DNAm platforms
445 (WGBS for the NBL training model and RRBS for the EWS samples), the inferred promoter
446 activity landscape was accurate ($R^2 = 0.718, 0.628$, and 0.702 for the three samples with HM
447 profiles, using leave-one-out prediction) (Additional file 2: Table S12).

448 Ewing sarcomas with mutations in *TP53* and *STAG2* have a particularly dismal prognosis
449 [63]. We explored whether the promoter activity had additional prognostic value in 72 samples
450 for which survival data was available. Because of the limited sample size, the initial analysis
451 revealed a significant association between poor clinical outcomes and *TP53* mutations
452 ($P = 0.00047$, log-rank test) (Additional file 1: Figure S12a) but not *STAG2* mutations
453 ($P = 0.67$, log-rank test) (Additional file 1: Figure S12b). We identified 21 active genes that
454 showed a potential difference (absolute mean difference of log-scaled activity ≥ 1) between
455 *TP53* mutant tumors and wild-type tumors, and we applied Cox proportional hazards models to
456 evaluate their potential contributions to patient survival that are independent of *TP53* or *STAG2*
457 mutation status (Additional file 2: Table S13). We performed the same analysis for 45 genes
458 with potential different promoter usage in tumors with and without *TP53* mutations (Additional

459 file 2: Table S14). Finally, we derived a multivariate Cox proportional hazards model including
460 both *TP53* and *STAG2* mutation status, one candidate gene with differential promoter activity
461 (*CALCB*), and five candidate gene isoforms (*CASZ1*, ENST00000496432; *RET*,
462 ENST00000479913; *TEX40*, ENST00000328404; *TNS1*, ENST00000446903; and *SLC27A6*,
463 ENST00000508645), and we followed this with backwards stepwise model selection. The final
464 model (Figure 5b) revealed potential protective roles for one candidate transcript *TNS1*
465 (ENST00000446903), a marginally protective role for candidate transcript *RET*
466 (ENST00000479913), and a candidate transcript associated with a poor prognosis, *SLC27A6*
467 (ENST00000508645).

468 *TNS1* encodes the well-studied protein Tensin 1, and is involved in several key aspects of
469 cell function, including extracellular matrix formation, actin cytoskeleton formation, and signal
470 transduction [64, 65]. More recently, the up-regulation of *TNS1* in colorectal cancer was found to
471 be associated with poor overall survival in patients [66], although previous studies have shown
472 suppression of *TNS1* expression [67] is associated with metastatic cancers. Our results suggest
473 that *TNS1* is a candidate prognostic indicator for EWS. Further studies are needed to draw
474 more attention to the functional roles of these genes/transcripts in EWS progression.

475

476 **Discussion**

477 Although epigenetic studies in disease models (cell lines, xenografts, and organoids) and in a
478 limited number of primary tumor samples have demonstrated the oncogenic contributions of
479 epigenetic deregulations to cancer initiation, progression, and response to treatment [48, 68, 69],
480 genome-wide profiling of promoter activities by using standard approaches (e.g., ChIP-seq or
481 CAGE) has not been carried out in large patient tumor cohorts, despite the continuous efforts of
482 large epigenome consortia [45, 46, 70]. Our analyses of *MYCN*-amplified NBL tumors revealed

483 both commonly active promoters and promoters that were active in some tumors but not in
484 others. Moreover, these sample-specific active promoters are functionally important, as they
485 drive the expression of several cancer consensus genes, including *MYC*. This observation is
486 consistent with recent reports of heterogeneous enhancer activities of cell line–defined super-
487 enhancers in primary gastric cancers [71], emphasizing the critical importance of deriving
488 sample-specific epigenomic signatures. To bridge the gap between the extensive epigenomic
489 resources in disease models and the limited ChIP-seq profiles of primary patient tumors, we
490 developed MethylationToActivity (M2A), a deep-learning framework, to characterize the
491 promoter activity landscape (both H3K4me3 and H3K27ac levels) in individual tumors by using
492 DNAm data, which is the most extensively documented epigenetic modification for patient
493 tumors and can be robustly and accurately profiled in FFPE archived retrospective samples.
494 M2A demonstrated excellent performance across various tumor types, with accuracy
495 comparable to that of ChIP-seq measurements of replicate samples from high-quality cohorts
496 (Figure 3).

497 Although our framework was strictly trained on HM levels, the inferred promoter activity was
498 highly correlated with the transcript-based gene expression levels quantified by RNA-seq
499 (Additional file 2: Tables S5, S7 and S8). The correlation between gene expression and inferred
500 promoter activities (mean $R^2 = 0.668$ for ENCODE data, 0.722 for K562, 0.705 for GM12878,
501 and 0.536 for H1-ESC) surpassed that with the state-of-art BPR model [42], which was
502 developed for predicting gene expression levels from DNAm patterns (the best reported R^2
503 values were 0.49 for K562, 0.37 for GM12878, and 0.25 for H1-ESC). Strikingly, the (indirect)
504 predictive accuracy of M2A for gene expression across nine ENCODE cell lines (average $R^2 =$
505 0.668) was comparable to the predictive accuracy of a model built on 11 HMs, one histone
506 variant, and DNase I hypersensitivity [11]. Similarly, the accuracy of binary prediction of
507 expressed genes (average AUC = 0.941 and 0.931 for the ENCODE and AML datasets,

508 respectively) surpassed that of DeepChrome (average AUC = 0.80), a state-of-art deep-learning
509 algorithm trained to predict expressed genes by using five core HMs (H3K4me3, H3K4me1,
510 H3K36me3, H3K9me3, and H3K27me3) [12]. These results further validated our framework.
511 Finally, both the M2A and BRP models suggest that it is insufficient to represent DNAm
512 information by using a simple average methylation level in the promoter region. To properly
513 reveal the regulatory roles of DNAm, we need to derive high-order features that capture spatial
514 relations among CpG probes (or window-based derived features calculated from them) in
515 promoters and in their vicinity. M2A uses the feature learning and selection characteristics of
516 CNNs to achieve its exceptional performance, thus demonstrating the rich information content of
517 DNAm signatures at both the genome-wide and local gene levels.

518 Analysis of the deep-learning framework revealed that M2A derives 1) high-level features
519 from DNAm patterns that are common among different tumors and 2) tumor subtype–specific
520 mapping functions from the mapping of high-level DNAm features to promoter activities in
521 individual tumor subtypes by using transfer learning (when feasible). Although our deep-learning
522 model cannot establish a causal relation between DNAm and promoter activities, these findings
523 nevertheless shed light on both the general and tumor subtype–specific rules for interpreting
524 DNAm patterns.

525 In evaluating our predictions, we found that several samples (the “poor performers”) showed
526 abnormally low predictive accuracy with both the ENCODE and BLUEPRINT datasets.
527 Investigations of the promoter H3K27ac levels revealed that the fraction of active promoters in
528 these samples was substantially lower than in other samples. Furthermore, joint analyses with
529 RNA-seq data from the matching samples indicated that 1) in contrast to the predictive accuracy
530 of H3K27ac levels, the “poor performers” achieved comparable consistency between the M2A-
531 inferred promoter activity and gene expression; 2) the “poor performers” showed significantly
532 lower correlation between the measured promoter H3K27ac level and gene expression; 3) the

533 correlation between the measured promoter H3K27ac level and gene expression was highly
534 predictive of the accuracy of the H3K27ac prediction (Additional file 1: Figure S10), and 4) in
535 ENCODE samples with replicates, the replicate with better consistency between H3K27ac and
536 gene expression also showed significantly higher correlation between the actual and measured
537 H3K27ac level ($P = 0.0039$, Wilcoxon signed rank test, Additional file 2: Table S15, an example
538 of H3K27ac signal discrepancy between H1-ESC replicates shown in Additional file 1: Figure
539 S8d). Although we cannot unequivocally rule out the possibility that these “poor performers”
540 share a distinct biological mechanism where promoter H3K27ac level is no longer a stronger
541 predictor for gene activities, these results suggested that the “poor performers” could reflect the
542 quality of the ChIP-seq results included in the test data. This observation emphasizes the value
543 of conducting a preliminary analysis to evaluate the data quality before incorporating public data.
544 It also suggests that M2A can provide a robust surrogate for promoter activities when the ChIP-
545 seq experimental data is questionable.

546 Alternative promoter usage increases the transcriptomic diversity during normal tissue
547 development and oncogenesis. Recent work demonstrated that an alternative promoter of
548 *ERBB2* is predictive of a poor clinical outcome but that the canonical promoter shows no
549 significant association with survival in patients with low-grade glioma [2]. Whereas earlier
550 studies focused on identifying alternative promoter usage through CAGE or RNA-seq data, our
551 research has shown that alternative promoter usage can be extensively studied by using DNAm
552 profiles from diverse samples, including retrospective FFPE tumor samples, for which traditional
553 approaches (CAGE, ChIP-seq, and RNA-seq) are technically challenging. Our analysis of a
554 large EWS cohort (without matching RNA-seq data) revealed promoter activities for several
555 specific isoforms that are independently associated with clinical outcomes, including a specific
556 isoform of the *TNS1* gene (ENST00000446903). This demonstrates the importance of analyzing
557 alternative promoter usage in epigenomic studies.

558 Finally, our analysis quantitatively emphasizes that promoter activity is one of the
559 mechanisms that regulate the final transcriptional output: 1) both the observed and predicted
560 promoter activities account for 50%–70% of the variation in gene expression, and 2)
561 approximately 40% of the genes differentially expressed in ERMS and ARMS tumors show
562 significant differences in their promoter activities. In addition to promoter activities, other
563 epigenetic mechanisms, including enhancer activities, contribute substantially to gene regulation
564 [72]. Recent work has demonstrated the roles of DNAm in regulating enhancer activities [73]
565 and aberrant cancer-specific DNAm patterns in super-enhancers [74]. Consequently, we aim to
566 expand our M2A framework to infer enhancer activities from DNAm patterns in the future.

567

568 **Conclusion**

569 We have demonstrated that MethylationToActivity overcomes the unique challenges of
570 systematically characterizing promoter activities from DNA methylation signatures. It achieved
571 an accurate, robust and generalizable performance in various pediatric and adult cancers,
572 including both solid and hematologic malignant neoplasms. MethylationToActivity will serve as a
573 valuable tool to provide functional interpretation of DNAm deregulation, characterize promoter
574 activity differences from DNAm patterns, and reveal alternate promoter usage in patient tumors,
575 which will facilitate precision medicine by tailoring treatments based on both genetic variants
576 and epigenetic deregulation.

577

578 **Methods**

579 **Datasets**

580 Five separate publicly available datasets were used in this study, including a pediatric NBL O-
581 PDX dataset ($N=16$) [40]; an RMS O-PDX dataset ($N=16$) [42]; ENCODE datasets with
582 matching H3K27ac and H3K4me3 histone mark ChIP-seq, RNA-seq, and WGBS experimental
583 data ($N=9$) [43]; a DCC BLUEPRINT AML dataset ($N=19$) [44]; and a pediatric EWS
584 dataset ($N=140$) [19] (Additional file 2: Table S16). Of the 140 samples in the EWS cohort,
585 only three had matching ChIP-seq and reduced-representation bisulfite sequencing (RRBS)
586 data available; for the remaining 137 samples, only RRBS data was available. All other cohort
587 datasets (i.e., the RMS, NBL, ENCODE, and AML datasets) contained matching H3K27ac and
588 H3K4me3 profiles, along with RNA-seq and WGBS experimental data.

589

590 **Feature processing**

591 All datasets were evaluated using GENCODE annotation definitions (www.gencodegenes.org/);
592 the NBL, RMS, ENCODE, and EWS datasets were evaluated using GENCODE GRCh37.p13
593 (release 19), and the AML dataset was evaluated using GENCODE GRCh38.p13 (release 32).
594 Promoter regions are defined as the TSS ± 1 kbp, where the TSS is defined as each unique
595 transcript start position. To avoid using identical or near-identical promoter regions in training
596 and baseline performance, only TSSs with promoter regions with less than 50% overlap were
597 considered. Gene orientation was taken into account, and any promoters with overlying regions
598 but opposite orientations were not considered as overlapping. Because of differences in sex
599 amongst samples, all chromosome X and Y promoter regions were removed from consideration.
600 This resulted in a total of 96,756 and 104,722 non-overlapping promoter regions from the
601 annotation files GRCh37.p13 and GRCh38.p13, respectively. For gene expression analysis, we
602 followed the definition in [11] and retained all 141,152 and 147,980 autosomal promoters for
603 protein-coding genes from the annotation files GRCh37.p13 and GRCh38.p13, respectively.

604 M2A uses only one variable feature type: DNA methylation. For WGBS/RRBS data, the M-value
605 was calculated as follows:

606

$$Mval_k = \log_2 \left(\frac{Methylated_k + \alpha}{Unmethylated_k + \alpha} \right),$$

607

608 where $Methylated_k$ and $Unmethylated_k$ correspond to the number of methylated and unmethylated
609 reads of the k^{th} CpG site, respectively. By default, the offset α was set to 0.5, and a global M-value
610 threshold was set to a maximum value of $\log_2(65)$ and a minimum value of $\log_2(\frac{1}{65})$. CpG sites with
611 coverage of less than five reads were removed.

612 M2A uses a promoter region-based windowed approach, comprising 20 windows of two sizes (250
613 bp and 2.5 kbp) and a step size equal to the window size, centered on a given TSS. For instance,
614 $W_{ij} = \{W_{i1}, W_{i2}, W_{i3} \dots, W_{i20}\}$ is the vector of windows where i represents a particular TSS and j
615 represents a particular window corresponding with the i^{th} TSS. This means that W_{i10} and W_{i11}
616 represent the windows immediately downstream and upstream of the i^{th} TSS. Therefore,
617

$$W_{i1} = TSS_i - 10^{th} \text{ window},$$

618

$$W_{i2} = TSS_i - 9^{th} \text{ window}, \dots$$

620

$$W_{i19} = TSS_i + 9^{th} \text{ window},$$

621

$$W_{i20} = TSS_i + 10^{th} \text{ window}$$

622

623 Each feature was calculated in this manner. The DNA methylation features, including the windowed
624 M-value mean, variance, and the fraction of the SSD of M-values (FSSD), were calculated and

625 represented by the feature vectors $Mave_i$, $Mvar_i$, and $Mfssd_i$. Therefore, the features for a particular
626 window, denoted as W_{ij} , would be calculated as follows:

$$Mave_{ij} = \frac{1}{n_{ij}} \sum Mval_{ik(j)},$$

$$Mvar_{ij} = \frac{1}{n_{ij}} \sum (Mave_{ij} - Mval_{ik(j)})^2,$$

627 and

$$Mfssd_{ij} = \frac{Mssd_{ij}}{\sum (Mave_i - Mval_k)^2},$$

628 where

$$Mave_i = \frac{1}{n_i} \sum Mval_k.$$

629 and

$$Mssd_{ij} = \sum (Mave_{ij} - Mval_{ik(j)})^2,$$

631

632 Here, i represents the promoter, j represents a specific window for a particular promoter, and
633 $Mval_k$ represents the Mval for individual CpGs in a region where $Mval_{k(j)}$ is the Mval for an individual
634 CpG in a specific window. Each feature was interleaved by window size to provide model input wherein
635 each window contained a number of “channels” equal to the number of features, with the feature array
636 shape being $(N, 2, 20, 3)$, where N represents the total number of TSSs in a sample, 2 represents the
637 number of window sizes (250 bp and 2.5 kbp), 20 represents the number of windows, and 3 represents
638 the number of features per window. All features were scaled from 0.1 to 1 (using MinMaxScaler with
639 default values from sklearn version 0.22); in instances where windows overlapped regions without
640 methylation data, resulting in NaNs (such as chromosomal boundaries, telomeric regions, and
641 centromeric regions), these feature values were marked as 0.

642

643 **Calculating histone modification enrichment**

644 The response variable was calculated for each non-overlapping promoter region, a 2000-bp region
645 centered on each TSS. Histone modification enrichment (HM) for the i^{th} promoter region is calculated
646 as follows:

$$HM_i = \log_2 \frac{\sum_k ChIP_{ik} + \alpha}{\sum_k Input_{ik} + \alpha},$$

647
648 where $\sum_k ChIP_{ik}$ represents the sum of either the H3K27ac or the H3K4me3 read signal mapped to the
649 promoter region at each position, $\sum_k Input_{ik}$ represents the sum of the control read signal mapped to
650 the promoter region, and α represents the 25th percentile of the $\sum_k Input_{ik}$ calculated for a given
651 sample.

652

653 **M2A topology**

654 M2A is a machine learning framework that leverages canonical deep-learning strategies, including
655 convolutional neural network (CNN) and fully connected (FC) layers. Each layer employs a LeakyReLU
656 (alpha=0.1) and a kernel constraint by L2-normalization using maxnorm(3). CNN layers are two-
657 dimensional, with zero padding, a stepsize of (1,1), and a kernel size of (1, 3) to maintain feature space
658 and prevent convolutions across features from different window sizes. To test the efficacy of this
659 approach, we compared the performance of a traditional artificial neural network (ANN) consisting of
660 two FC layers versus three CNN layers in addition to two FC layers. During transfer learning, weights
661 corresponding to each of the three CNN layers of the six–NBL O-PDX M2A model trained previously
662 were frozen; only the weights corresponding to the two FC layers were optimized. A summary of all
663 model topologies and parameters can be found in Additional file 2: Table S17. To train and test each
664 model topology, we used Keras (v2.2.4) and Tensorflow (v2.1.0) in Python 3.6.5.

665

666 **M2A parameter tuning**

667 Parameters such as the window size, batch size, and kernel size were optimized using the validation
668 NBL data set (n=10). Each parameter configuration was tested holding all other parameters constant,
669 and models with a numerical performance advantage were chosen. For batch size, three configurations
670 were tested (64, 128, 256). Four kernel size configurations ([1,2], [1,3], [1,4], [1,5]) were tested. and
671 window configurations ([100bp, 1000bp], [250bp, 2500bp], [500bp, 5000bp]) were considered. Due
672 to >50% uninformative features in the 100bp window resolution, only the (250bp, 2500bp) model and
673 (500bp, 5000bp) model performances were compared (Additional file 1: Figure S13; Additional file 2:
674 Table S18).

675

676 **Training M2A**

677 The core M2A model (without transfer) training set consisted of six O-PDX samples from the 16-
678 sample NBL cohort (Additional file 2: Table S19); we trained separate models for H3K27ac and
679 H3K4me3 HMs with the same WGBS features as the input. After the base models were trained,
680 transfer learning was employed for three separate datasets, namely the RMS, AML, and EWS
681 datasets. Each transfer learning model was trained using one sample from the cohort, for a total
682 of N models, where N equals the number of samples in the cohort. For the RMS and EWS
683 cohorts, an ensemble approach was used, whereby an averaged prediction from N-1 models
684 was generated after transfer learning with each sample. The same approach was used with the
685 AML cohort, except that only samples with $R^2 \geq 0.60$ between FPKM and H3K27ac were used
686 for transfer learning.

687 For each training scheme, the same parameters were used, including an 80/20 training/validation
688 split and a batch size of 64 (Additional file 2: Table S17). All sample input was randomized before
689 training. The Keras implementation of adadelta (default parameters) minimizing the mean squared error
690 (MSE) was used to optimize M2A. To prevent overtraining, the EarlyStopping method was employed by
691 monitoring validation loss for 10 epochs without at least a minimal gain in performance (min_delta =
692 0.0001) for a maximum of 80 epochs. In no case was the maximum number of epochs reached.

693

694 **Determining promoter diversity in NBL models**

695 Promoter region-based H3K27ac distributions clearly show a bimodal distribution (see
696 Additional file 1: Figure S1); therefore, to determine class occupancy (active versus inactive), a
697 Gaussian mixture model (GaussianMixture from sklearn version 0.22 with n_components = 2)
698 was applied for each individual sample. To determine the percentage of differentially active
699 promoters among all active promoters, we used a pairwise comparison approach for all samples.
700 Cancer consensus genes were downloaded from COSMIC (<https://cancer.sanger.ac.uk/census>)
701 (accessed on February 1, 2020). To avoid artificially inflated values from genes with multiple
702 TSSs, only cancer consensus genes with a single TSS according to GENCODE GRCh37.p13
703 (release 19) definitions were considered.

704

705 **Evaluating M2A performance**

706 When determining prediction performance, two primary metrics were considered, namely the R^2 and
707 the root mean squared error (RMSE). To measure the accuracy of M2A in predicting expressed genes,
708 we calculated the AUC-ROC by using roc_curve and the precision-recall curve AUC by using
709 average_precision_score from sklearn 0.22. Paired analyses were tested for statistical significance by
710 using a Wilcoxon signed-rank test (R v3.4.1). To determine outliers, a median-based method was
711 implemented using the “outlier” function in the R package GmAMisc [55]. To ensure that low-
712 mappability regions were not a confounding factor, we used the
713 wgEncodeCrgMApabilityAlign100mer.bw file downloaded from the UCSC Genome Browser
714 (<http://genome.ucsc.edu/cgi-bin/hgFileUi?db=hg19&g=wgEncodeMapability>). For GRCh38.p13
715 annotations, we used liftOver from UCSC (http://hgdownload.cse.ucsc.edu/admin/exe/linux.x86_64/) to
716 convert the mappability track to GRCh38. For all performance-related analyses, the average value of

717 this track within each non-overlapping 2000-bp promoter region was calculated, and promoter regions
718 with mappability > 0.75 were retained for evaluation.

719 In analyses between H3K27ac levels (actual or predicted) and gene expression, we followed the
720 gene filtering steps described in [11]: all autosomal protein-coding gene promoters were considered
721 and for genes with multiple promoters, we use the maximum promoter activity to represent the gene.

722

723 **Baseline models**

724 Multivariate adaptive regression splines (MARS) was implemented by “earth” package in R (all default
725 values were used), and the random forest baseline model was implemented by the
726 “sklearn.ensemble.RandomForestRegressor” package in python 3.7.0 (max_features='sqrt'). For
727 comparison purposes, each model tested used identical feature input to M2A.

728

729 **M2A captures the impact of DMRs on promoter region activity**

730 The lists of genes that are differentially expressed in ERMS and ARMS samples and genes with DMRs
731 were previously reported in reference [42].

732

733 **Alternative promoter usage analyses**

734 To infer alternative promoter usage that was specific to the RMS subtypes ARMS and ERMS, we first
735 delineated the “active” vs. “inactive” promoters in a subtype (ERMS or ARMS) by applying a threshold
736 of $mean(H3K27ac) > 1$ for the average samples in the subtype. Next, primary promoters from multi-
737 promoter genes were determined by the average H3K27ac level within a specific subtype, and the
738 promoter with the maximum activity from a given gene was counted as the primary promoter. The
739 differences in promoter usage between two subtypes was defined as the difference between the activity
740 sum of the primary promoters and the activity sum of the secondary promoters in the two subtypes.

741

742 **Analysis of alternative promoter usage in EWS**

743 In the same manner as the RMS subtype analysis, EWS alternative promoter usage was determined in
744 two patient sample groups: *TP53* mutant and *TP53* wild-type groups (for sample status, see Additional
745 file 2: Table S18). Candidate genes were identified as active genes ($H3K27ac \geq 1$ in at least one group)
746 with potential differential promoter activities (absolute difference ≥ 1) in the *TP53* wild-type and *TP53*
747 mutant groups. Candidate genes with alternative promoter usage were identified as genes that used
748 different active primary promoters in the wild-type and mutant groups and had an average promoter
749 usage difference of at least 0.4 between groups. Both alternative promoters and differentially active
750 promoters were considered in prognostic analyses (univariate screening incorporating both *TP53* and
751 *STAG2* mutation status, followed by a multivariate analysis) using Cox proportional hazard models (R
752 3.4.1). The final model was derived from backward stepwise selection from a Cox proportional hazards
753 model including *TP53* and *STAG2* mutation status and all potential markers (all genes or promoters
754 with an FDR < 0.05 in the univariate analysis).

755

756 **Analysis of M2A feature input and extracted features**

757 To determine the merit of a CNN-based approach, each feature average for a particular window
758 position and window size were plotted with a 95% confidence interval. The plotted feature distribution
759 was calculated from all M2A vanilla model training data input (NBL, N=6), and stratified by promoter
760 status. Promoter status was determined by class occupancy of both $H3K27ac$ and $H3K4me3$, (active
761 versus inactive), where ($H3K27ac=active$), ($H3K27ac=inactive$, $H3K4me3=active$), and
762 ($H3K27ac=inactive$, $H3K4me3=inactive$), represents active, poised, and inactive promoters,
763 respectively. Class occupancy was determined by applying a Gaussian mixture model
764 (GaussianMixture from sklearn version 0.22 with $n_components = 2$).

765 The efficacy of the CNN-based feature extraction was tested by 1) training sample input feature
766 predictive performance as compared to CNN-extracted feature performance, calculated by Pearson's

767 R^2 for all features across the entire training set (each window size considered separately; NBL, N=6)
768 and 2) The performance (Pearson's R^2) of the best performing feature identified in 1) when applied to
769 each sample in the validation set (NBL, N=10; Additional File 1: Figure S3).

770

771 **M2A code availability**

772 The latest M2A models, feature generation, prediction pipeline, and a Docker image of the M2A
773 environment pre-loaded are available for download at <https://github.com/chenlab-sj/M2A>. Additionally,
774 source code with detailed instructions for transfer learning using the M2A model with input samples
775 from other domains is available. The cloud-based implementation of M2A is available to anyone with a
776 (free) St. Jude Cloud account (<https://platform.stjude.cloud/workflows/methylation-to-activity>).

777

778 **Declarations**

779 **Ethics approval and consent to participate**

780 Not applicable

781 **Consent for publication**

782 Not applicable

783 **Availability of data and materials**

784 The datasets generated and/or analyzed during the current study are publicly available, as detailed in
785 Additional File 2: Table S16.

786 **Competing interests**

787 The authors declare that they have no known competing financial interests or personal relationships
788 that could have appeared to influence the work reported in this paper.

789 **Funding**

790 National Cancer Institute of the National Institutes of Health [P30CA021765]; American Lebanese
791 Syrian Associated Charities (ALSAC). The content is solely the responsibility of the authors and does
792 not necessarily represent the official views of the National Institutes of Health.

793 **Authors' contributions**

794 **JW**: Methodology, software, data analysis, result interpretation, writing - original draft, writing - review &
795 editing. **BX**: Resources, data curation. **DP**: Software, resources. **AT**: Software, resources. **CL**: Result
796 interpretation, writing – review & editing. **JY**: Result interpretation, writing – review & editing. **XC**:
797 Conceptualization, methodology, data analysis, result interpretation, writing - review & editing,
798 supervision.

799 **Acknowledgements**

800 We thank Keith A. Laycock, PhD, ELS, for editing the manuscript.

801

802 **References**

- 803 1. Davuluri RV, Suzuki Y, Sugano S, Plass C, Huang TH: **The functional consequences of**
804 **alternative promoter use in mammalian genomes.** *Trends Genet* 2008, **24**:167-177.
- 805 2. Demircioglu D, Cukuroglu E, Kindermans M, Nandi T, Calabrese C, Fonseca NA,
806 Kahles A, Lehmann KV, Stegle O, Brazma A, et al: **A Pan-cancer Transcriptome**
807 **Analysis Reveals Pervasive Regulation through Alternative Promoters.** *Cell* 2019,
808 **178**:1465-1477 e1417.
- 809 3. Qamra A, Xing M, Padmanabhan N, Kwok JJT, Zhang S, Xu C, Leong YS, Lee Lim AP,
810 Tang Q, Ooi WF, et al: **Epigenomic Promoter Alterations Amplify Gene Isoform and**
811 **Immunogenic Diversity in Gastric Adenocarcinoma.** *Cancer Discov* 2017, **7**:630-651.
- 812 4. Sotillo E, Barrett DM, Black KL, Bagashev A, Oldridge D, Wu G, Sussman R, Lanauze
813 C, Ruella M, Gazzara MR, et al: **Convergence of Acquired Mutations and Alternative**
814 **Splicing of CD19 Enables Resistance to CART-19 Immunotherapy.** *Cancer Discov*
815 2015, **5**:1282-1295.
- 816 5. Ma X, Liu Y, Liu Y, Alexandrov LB, Edmonson MN, Gawad C, Zhou X, Li Y, Rusch
817 MC, Easton J, et al: **Pan-cancer genome and transcriptome analyses of 1,699**
818 **paediatric leukaemias and solid tumours.** *Nature* 2018, **555**:371-376.
- 819 6. Grobner SN, Worst BC, Weischenfeldt J, Buchhalter I, Kleinheinz K, Rudneva VA,
820 Johann PD, Balasubramanian GP, Segura-Wang M, Brabetz S, et al: **The landscape of**
821 **genomic alterations across childhood cancers.** *Nature* 2018, **555**:321-327.

822 7. Huether R, Dong L, Chen X, Wu G, Parker M, Wei L, Ma J, Edmonson MN, Hedlund
823 EK, Rusch MC, et al: **The landscape of somatic mutations in epigenetic regulators**
824 **across 1,000 paediatric cancer genomes.** *Nat Commun* 2014, **5**:3630.

825 8. Andersson R, Sandelin A: **Determinants of enhancer and promoter activities of**
826 **regulatory elements.** *Nat Rev Genet* 2020, **21**:71-87.

827 9. Kelley DZ, Flam EL, Izumchenko E, Danilova LV, Wulf HA, Guo T, Singman DA,
828 Afsari B, Skaist AM, Considine M, et al: **Integrated Analysis of Whole-Genome ChIP-**
829 **Seq and RNA-Seq Data of Primary Head and Neck Tumor Samples Associates HPV**
830 **Integration Sites with Open Chromatin Marks.** *Cancer Res* 2017, **77**:6538-6550.

831 10. Karlic R, Chung HR, Lasserre J, Vlahovicek K, Vingron M: **Histone modification levels**
832 **are predictive for gene expression.** *Proc Natl Acad Sci U S A* 2010, **107**:2926-2931.

833 11. Dong X, Greven MC, Kundaje A, Djebali S, Brown JB, Cheng C, Gingeras TR, Gerstein
834 M, Guigo R, Birney E, Weng Z: **Modeling gene expression using chromatin features**
835 **in various cellular contexts.** *Genome Biol* 2012, **13**:R53.

836 12. Singh R, Lanchantin J, Robins G, Qi Y: **DeepChrome: deep-learning for predicting**
837 **gene expression from histone modifications.** *Bioinformatics* 2016, **32**:i639-i648.

838 13. Kaghohara LT, Stein-O'Brien GL, Kelley D, Flam E, Wick HC, Danilova LV, Easwaran H,
839 Favorov AV, Qian J, Gaykalova DA, Fertig EJ: **Epigenetic regulation of gene**
840 **expression in cancer: techniques, resources and analysis.** *Brief Funct Genomics* 2018,
841 **17**:49-63.

842 14. Zhang P, Lehmann BD, Shyr Y, Guo Y: **The Utilization of Formalin Fixed-Paraffin-**
843 **Embedded Specimens in High Throughput Genomic Studies.** *Int J Genomics* 2017,
844 **2017**:1926304.

845 15. Moran S, Vizoso M, Martinez-Cardus A, Gomez A, Matias-Guiu X, Chiavenna SM,
846 Fernandez AG, Esteller M: **Validation of DNA methylation profiling in formalin-fixed**
847 **paraffin-embedded samples using the Infinium HumanMethylation450 Microarray.**
848 *Epigenetics* 2014, **9**:829-833.

849 16. de Ruijter TC, de Hoon JP, Slaats J, de Vries B, Janssen MJ, van Wezel T, Aarts MJ, van
850 Engeland M, Tjan-Heijnen VC, Van Neste L, Veeck J: **Formalin-fixed, paraffin-**
851 **embedded (FFPE) tissue epigenomics using Infinium HumanMethylation450**
852 **BeadChip assays.** *Lab Invest* 2015, **95**:833-842.

853 17. Gu H, Bock C, Mikkelsen TS, Jager N, Smith ZD, Tomazou E, Gnirke A, Lander ES,
854 Meissner A: **Genome-scale DNA methylation mapping of clinical samples at single-**
855 **nucleotide resolution.** *Nat Methods* 2010, **7**:133-136.

856 18. Ziller MJ, Gu H, Muller F, Donaghey J, Tsai LT, Kohlbacher O, De Jager PL, Rosen ED,
857 Bennett DA, Bernstein BE, et al: **Charting a dynamic DNA methylation landscape of**
858 **the human genome.** *Nature* 2013, **500**:477-481.

859 19. Charlet J, Duymich CE, Lay FD, Mundbjerg K, Dalsgaard Sorensen K, Liang G, Jones
860 PA: **Bivalent Regions of Cytosine Methylation and H3K27 Acetylation Suggest an**
861 **Active Role for DNA Methylation at Enhancers.** *Mol Cell* 2016, **62**:422-431.

862 20. Onuchic V, Lurie E, Carrero I, Pawliczek P, Patel RY, Rozowsky J, Galeev T, Huang Z,
863 Altshuler RC, Zhang Z, et al: **Allele-specific epigenome maps reveal sequence-**
864 **dependent stochastic switching at regulatory loci.** *Science* 2018, **361**.

865 21. Stadler MB, Murr R, Burger L, Ivanek R, Lienert F, Scholer A, van Nimwegen E,
866 Wirbelauer C, Oakeley EJ, Gaidatzis D, et al: **DNA-binding factors shape the mouse**
867 **methylome at distal regulatory regions.** *Nature* 2011, **480**:490-495.

868 22. Sheffield NC, Pierron G, Klughammer J, Datlinger P, Schonegger A, Schuster M, Hadler
869 J, Surdez D, Guillemot D, Lapouble E, et al: **DNA methylation heterogeneity defines a**
870 **disease spectrum in Ewing sarcoma.** *Nat Med* 2017, **23**:386-395.

871 23. Zhu H, Wang G, Qian J: **Transcription factors as readers and effectors of DNA**
872 **methylation.** *Nature Reviews Genetics* 2016, **17**:551-565.

873 24. Kondo Y: **Epigenetic cross-talk between DNA methylation and histone modifications**
874 **in human cancers.** *Yonsei Med J* 2009, **50**:455-463.

875 25. Rothbart SB, Strahl BD: **Interpreting the language of histone and DNA modifications.**
876 *Biochim Biophys Acta* 2014, **1839**:627-643.

877 26. Hashimshony T, Zhang J, Keshet I, Bustin M, Cedar H: **The role of DNA methylation**
878 **in setting up chromatin structure during development.** *Nat Genet* 2003, **34**:187-192.

879 27. Moore LD, Le T, Fan G: **DNA methylation and its basic function.**
880 *Neuropsychopharmacology* 2013, **38**:23-38.

881 28. Jenkinson G, Pujadas E, Goutsias J, Feinberg AP: **Potential energy landscapes identify**
882 **the information-theoretic nature of the epigenome.** *Nat Genet* 2017, **49**:719-729.

883 29. Fortin JP, Hansen KD: **Reconstructing A/B compartments as revealed by Hi-C using**
884 **long-range correlations in epigenetic data.** *Genome Biol* 2015, **16**:180.

885 30. Simmonds P, Loomis E, Curry E: **DNA methylation-based chromatin compartments**
886 **and ChIP-seq profiles reveal transcriptional drivers of prostate carcinogenesis.**
887 *Genome Med* 2017, **9**:54.

888 31. Mack SC, Witt H, Piro RM, Gu L, Zuyderduyn S, Stutz AM, Wang X, Gallo M, Garzia L,
889 Zayne K, et al: **Epigenomic alterations define lethal CIMP-positive ependymomas of**
890 **infancy.** *Nature* 2014, **506**:445-450.

891 32. Teodoridis JM, Hardie C, Brown R: **CpG island methylator phenotype (CIMP) in**
892 **cancer: causes and implications.** *Cancer Lett* 2008, **268**:177-186.

893 33. Capper D, Jones DTW, Sill M, Hovestadt V, Schrimpf D, Sturm D, Koelsche C, Sahm F,
894 Chavez L, Reuss DE, et al: **DNA methylation-based classification of central nervous**
895 **system tumours.** *Nature* 2018, **555**:469-474.

896 34. Perez E, Capper D: **Invited Review: DNA methylation-based classification of**
897 **paediatric brain tumours.** *Neuropathol Appl Neurobiol* 2020.

898 35. Strahl BD, Allis CD: **The language of covalent histone modifications.** *Nature* 2000,
899 **403**:41-45.

900 36. Musselman CA, Lalonde ME, Cote J, Kutateladze TG: **Perceiving the epigenetic**
901 **landscape through histone readers.** *Nat Struct Mol Biol* 2012, **19**:1218-1227.

902 37. Spainhour JC, Lim HS, Yi SV, Qiu P: **Correlation Patterns Between DNA**
903 **Methylation and Gene Expression in The Cancer Genome Atlas.** *Cancer Inform* 2019,
904 **18**:1176935119828776.

905 38. Baylin SB: **DNA methylation and gene silencing in cancer.** *Nature Clinical Practice*
906 *Oncology* 2005, **2**:S4-S11.

907 39. Jones PA: **Functions of DNA methylation: islands, start sites, gene bodies and**
908 **beyond.** *Nature Reviews Genetics* 2012, **13**:484-492.

909 40. Lay FD, Liu Y, Kelly TK, Witt H, Farnham PJ, Jones PA, Berman BP: **The role of DNA**
910 **methylation in directing the functional organization of the cancer epigenome.**
911 *Genome Research* 2015, **25**:467-477.

912 41. Kagohara LT, Stein-O'Brien GL, Kelley D, Flam E, Wick HC, Danilova LV, Easwaran
913 H, Favorov AV, Qian J, Gaykalova DA, Fertig EJ: **Epigenetic regulation of gene**

914 expression in cancer: techniques, resources and analysis. *Briefings in Functional*
915 *Genomics* 2018, **17**:49-63.

916 42. Kapourani CA, Sanguinetti G: **Higher order methylation features for clustering and**
917 **prediction in epigenomic studies.** *Bioinformatics* 2016, **32**:i405-i412.

918 43. Zeineldin M, Federico S, Chen X, Fan Y, Xu B, Stewart E, Zhou X, Jeon J, Griffiths L,
919 Nguyen R, et al: **MYCN amplification and ATRX mutations are incompatible in**
920 **neuroblastoma.** *Nat Commun* 2020, **11**:913.

921 44. Stewart E, McEvoy J, Wang H, Chen X, Honnell V, Ocarz M, Gordon B, Dapper J,
922 Blankenship K, Yang Y, et al: **Identification of Therapeutic Targets in**
923 **Rhabdomyosarcoma through Integrated Genomic, Epigenomic, and Proteomic**
924 **Analyses.** *Cancer Cell* 2018.

925 45. Consortium EP: **An integrated encyclopedia of DNA elements in the human genome.**
926 *Nature* 2012, **489**:57-74.

927 46. Stunnenberg HG, International Human Epigenome C, Hirst M: **The International**
928 **Human Epigenome Consortium: A Blueprint for Scientific Collaboration and**
929 **Discovery.** *Cell* 2016, **167**:1145-1149.

930 47. Singh AA, Schuurman K, Nevedomskaya E, Steloo S, Linder S, Droog M, Kim Y,
931 Sanders J, van der Poel H, Bergman AM, et al: **Optimized ChIP-seq method facilitates**
932 **transcription factor profiling in human tumors.** *Life Sci Alliance* 2019, **2**:e201800115.

933 48. Seligson DB, Horvath S, Shi T, Yu H, Tze S, Grunstein M, Kurdistani SK: **Global**
934 **histone modification patterns predict risk of prostate cancer recurrence.** *Nature*
935 2005, **435**:1262-1266.

936 49. Chen X, Stewart E, Shelat AA, Qu C, Bahrami A, Hatley M, Wu G, Bradley C, McEvoy
937 J, Pappo A, et al: **Targeting oxidative stress in embryonal rhabdomyosarcoma.**
938 *Cancer Cell* 2013, **24**:710-724.

939 50. Stewart E, Shelat A, Bradley C, Chen X, Federico S, Thiagarajan S, Shirinifard A,
940 Bahrami A, Pappo A, Qu C, et al: **Development and characterization of a human**
941 **orthotopic neuroblastoma xenograft.** *Dev Biol* 2015, **407**:344-355.

942 51. Stewart E, Federico SM, Chen X, Shelat AA, Bradley C, Gordon B, Karlstrom A,
943 Twarog NR, Clay MR, Bahrami A, et al: **Orthotopic patient-derived xenografts of**
944 **paediatric solid tumours.** *Nature* 2017, **549**:96-100.

945 52. Murphy AJ, Chen X, Pinto EM, Williams JS, Clay MR, Pounds SB, Cao X, Shi L, Lin T,
946 Neale G, et al: **Forty-five patient-derived xenografts capture the clinical and**
947 **biological heterogeneity of Wilms tumor.** *Nat Commun* 2019, **10**:5806.

948 53. Angermueller C, Lee HJ, Reik W, Stegle O: **DeepCpG: accurate prediction of single-**
949 **cell DNA methylation states using deep learning.** *Genome Biol* 2017, **18**:67.

950 54. Barredo Arrieta A, Díaz-Rodríguez N, Del Ser J, Bennetot A, Tabik S, Barbado A,
951 Garcia S, Gil-Lopez S, Molina D, Benjamins R, et al: **Explainable Artificial**
952 **Intelligence (XAI): Concepts, taxonomies, opportunities and challenges toward**
953 **responsible AI.** *Information Fusion* 2020, **58**:82-115.

954 55. Wilcox RR: **The Normal Curve and Outlier Detection.** In *Fundamentals of Modern*
955 *Statistical Methods.* 2001: 31-47

956 56. Golob JL, Kumar RM, Guenther MG, Pabon LM, Pratt GA, Loring JF, Laurent LC,
957 Young RA, Murry CE: **Evidence that gene activation and silencing during stem cell**
958 **differentiation requires a transcriptionally paused intermediate state.** *PLoS One*
959 2011, **6**:e22416.

960 57. Berdasco M, Esteller M: **Clinical epigenetics: seizing opportunities for translation.**
961 *Nat Rev Genet* 2019, **20**:109-127.

962 58. Hinoue T, Weisenberger DJ, Lange CPE, Shen H, Byun HM, Van Den Berg D, Malik S,
963 Pan F, Noushmehr H, van Dijk CM, et al: **Genome-scale analysis of aberrant DNA**
964 **methylation in colorectal cancer.** *Genome Research* 2011, **22**:271-282.

965 59. Cao L, Yu Y, Bilke S, Walker RL, Mayeenuddin LH, Azorsa DO, Yang F, Pineda M,
966 Helman LJ, Meltzer PS: **Genome-wide identification of PAX3-FKHR binding sites in**
967 **rhabdomyosarcoma reveals candidate target genes important for development and**
968 **cancer.** *Cancer research* 2010, **70**:6497-6508.

969 60. Laé M, Ahn E, Mercado G, Chuai S, Edgar M, Pawel B, Olshen A, Barr F, Ladanyi M:
970 **Global gene expression profiling of PAX-FKHR fusion-positive alveolar and PAX-**
971 **FKHR fusion-negative embryonal rhabdomyosarcomas.** *The Journal of Pathology*
972 2007, **212**:143-151.

973 61. Marshall AD, Grosveld GC: **Alveolar rhabdomyosarcoma – The molecular drivers of**
974 **PAX3/7-FOXO1-induced tumorigenesis.** *Skeletal Muscle* 2012, **2**:25.

975 62. Honda T, Inui M: **PDZRN3 regulates differentiation of myoblasts into myotubes**
976 **through transcriptional and posttranslational control of Id2.** *Journal of Cellular*
977 *Physiology* 2019, **234**:2963-2972.

978 63. Tirode F, Surdez D, Ma X, Parker M, Le Deley MC, Bahrami A, Zhang Z, Lapouble E,
979 Grosssetete-Lalami S, Rusch M, et al: **Genomic Landscape of Ewing Sarcoma Defines**
980 **an Aggressive Subtype with Co-Association of STAG2 and TP53 Mutations.** *Cancer*
981 *Discov* 2014, **4**:1342-1353.

982 64. Lo SH, An Q, Bao S, Wong WK, Liu Y, Janmey PA, Hartwig JH, Chen LB: **Molecular**
983 **cloning of chick cardiac muscle tensin. Full-length cDNA sequence, expression, and**
984 **characterization.** *J Biol Chem* 1994, **269**:22310-22319.

985 65. Chen H, Duncan IC, Bozorgchami H, Lo SH: **Tensin1 and a previously undocumented**
986 **family member, tensin2, positively regulate cell migration.** *Proc Natl Acad Sci U S A*
987 2002, **99**:733-738.

988 66. Zhou H, Zhang Y, Wu L, Xie W, Li L, Yuan Y, Chen Y, Lin Y, He X: **Elevated**
989 **transgelin/TNS1 expression is a potential biomarker in human colorectal cancer.**
990 *Oncotarget* 2018, **9**:1107-1113.

991 67. Hall EH, Daugherty AE, Choi CK, Horwitz AF, Brautigan DL: **Tensin1 requires**
992 **protein phosphatase-1alpha in addition to RhoGAP DLC-1 to control cell**
993 **polarization, migration, and invasion.** *J Biol Chem* 2009, **284**:34713-34722.

994 68. Shen H, Laird PW: **Interplay between the cancer genome and epigenome.** *Cell* 2013,
995 **153**:38-55.

996 69. De Craene B, Berx G: **Regulatory networks defining EMT during cancer initiation**
997 **and progression.** *Nat Rev Cancer* 2013, **13**:97-110.

998 70. Roadmap Epigenomics C, Kundaje A, Meuleman W, Ernst J, Bilenky M, Yen A, Heravi-
999 Moussavi A, Kheradpour P, Zhang Z, Wang J, et al: **Integrative analysis of 111**
1000 **reference human epigenomes.** *Nature* 2015, **518**:317-330.

1001 71. Ooi WF, Xing M, Xu C, Yao X, Ramlee MK, Lim MC, Cao F, Lim K, Babu D, Poon LF,
1002 et al: **Epigenomic profiling of primary gastric adenocarcinoma reveals super-**
1003 **enhancer heterogeneity.** *Nat Commun* 2016, **7**:12983.

1004 72. Pennacchio LA, Bickmore W, Dean A, Nobrega MA, Bejerano G: **Enhancers: five**
1005 **essential questions.** *Nat Rev Genet* 2013, **14**:288-295.

1006 73. Weigel C, Chaisaingmongkol J, Assenov Y, Kuhmann C, Winkler V, Santi I, Bogatyrova
1007 O, Kaucher S, Bermejo JL, Leung SY, et al: **DNA methylation at an enhancer of the**
1008 **three prime repair exonuclease 2 gene (TREX2) is linked to gene expression and**
1009 **survival in laryngeal cancer.** *Clin Epigenetics* 2019, **11**:67.

1010 74. Heyn H, Vidal E, Ferreira HJ, Vizoso M, Sayols S, Gomez A, Moran S, Boque-Sastre R,
1011 Guil S, Martinez-Cardus A, et al: **Epigenomic analysis detects aberrant super-**
1012 **enhancer DNA methylation in human cancer.** *Genome Biol* 2016, **17**:11.

1013

1014 **Figure Legends**

1015 **Figure 1 Variations of promoter H3K27ac levels among *MYCN* amplified NBL samples.**

1016 **(a–c)** Promoters were classified as active or inactive based on H3K27ac levels in individual NBL
1017 tumors: **(a)** NBL cell line samples, **(b)** NBL O-PDX samples, and **(c)** NBL cell line and O-PDX
1018 samples. Each promoter region plotted spans TSS \pm 5,000 bp binned by non-overlapping 250
1019 bp windows; the color bar represents the scaled windowed H3K27ac enrichment, from 0 (lowest)
1020 to 3 (highest). Horizontal dotted lines delineate shared promoters (active in all samples) and
1021 sample-specific promoters (promoter activity in at least one sample was different from the
1022 remaining samples). Promoters were sorted by average descending H3K27ac enrichment
1023 across all samples within each group. **(d, e)** Venn diagram indicating the number of shared and
1024 sample-specific H3K27ac promoter activities between NBL cell line samples **(d)** and O-PDX
1025 samples **(e)**. **(f)** The promoter activity variation is highlighted by the proportion of sample-
1026 specific active promoters among all H3K27ac active promoters, as compared within cell line or
1027 O-PDX NBL samples, and between cell line and O-PDX NBL samples.

1028

1029 **Figure 2. M2A feature processing and training workflow.**

1030 The M2A framework hinges on the feature processing pipeline. **(a)** First, windowed features (20
1031 total non-overlapping windows for each of two sizes including 250 bp and 2,500 bp) centered
1032 around the TSS are calculated from WGBS data for each unique promoter region, extending up
1033 to 2,500 bp (250 bp window), and 25 kbp (2,500 bp window) away from the TSS. Response

1034 variables (H3K27ac and H3K4me3) for separate model training were generated for matching
1035 promoter regions ($\text{TSS} \pm 1 \text{ kbp}$). The matching window features and response variables serve
1036 as input to the model topologies, where M2A first extracts high-level features by using a series
1037 of convolutional layers then maps these features to response variables in fully-connected (FC)
1038 layers. Transfer learning with M2A leverages pretrained feature extraction (frozen CNN layers
1039 indicated in blue), training only the FC layers. **(b)** The overall workflow for training, validation,
1040 and testing M2A is detailed, as well as an overview of the analyses performed to validate M2A
1041 performance in different real-world applications. M2A models for H3K4me3 and H3K27ac were
1042 trained separately, indicated by blue (H3K4me3) and green (H3K27ac).

1043

1044 **Figure 3. M2A performance in NBL and RMS cohorts.**

1045 **(a, b)** Analysis of the performance of M2A in NBL and RMS cohorts with **(a)** H3K4me3 inference
1046 and **(b)** H3K27ac inference. ENCODE replicate consistencies were calculated as Pearson's
1047 correlation squared (R^2) between replicates (two replicates per sample). ENCODE sample
1048 KMS-11 was excluded as an apparent outlier $R^2=0.016$, RMSE = 1.869. Prediction accuracy
1049 was measured by R^2 between the actual measurement and M2A's prediction. **(c-g)** Individual
1050 examples of median M2A performers in **(c)** NBL cell line H3K27ac inference, **(d)** NBL cell line
1051 H3K4me3 inference, **(e)** RMS H3K27ac inference (pre-transfer), **(f)** RMS H3K4me3 inference,
1052 and **(g)** RMS H3K27ac inference (post-transfer). To indicate the density of data points where
1053 individual data points cannot be resolved, a KDE was applied, called from 1 (highest) to 0
1054 (lowest). **(h)** The boost to M2A performance (measured by RMSE) due to transfer learning is
1055 shown, as applied and tested in RMS samples.

1056

1057 **Figure 4. M2A recapitulates subtype differences in RMS.**

1058 **(a)** A t-distributed Stochastic Neighbor Embedding (tSNE) analysis of observed (left), M2A
1059 inferred (center: pre-transfer, right: post-transfer) H3K27ac promoter levels. Embryonal and

1060 alveolar RMS subtypes are well separated in each analysis, demonstrating that M2A inferred
1061 H3K27ac levels maintain the delineation of RMS subtypes, consistent with the observed
1062 H3K27ac tSNE analysis. **(b-d)** The subtype-specific genes *GAS2* **(b)** and *NOS1* **(c)** show
1063 subtype distinct patterns of DNAm, H3K27ac, and H3K4me3 levels. The windowed average
1064 DNAm feature (2,500 bp windows, over the genomic region TSS \pm 25 kb) is shown as example
1065 (partial) M2A input. These subtype differences were faithfully recapitulated by the M2A
1066 H3K27ac inferences for *GAS2* **(d)** and *NOS1* **(e)**.

1067

1068 **Figure 5. M2A reveals alternate promoter usage in RMS and EWS.**

1069 **(a)** An analysis of alternate primary promoter usage between RMS subtypes ERMS and ARMS
1070 shows that M2A appropriately predicts subtype-specific promoter usage in *PDZRN3*, a known
1071 target of the PAX3/7-FOXO1 fusion protein, which is consistent at the observed values of
1072 H3K27ac, H3K4me3, RNA-seq, and DNA methylation. Partial M2A input (DNAm 2,500 bp
1073 windowed average) is shown to emphasize the DNAm patterns in the genomic region
1074 surrounding the TSS \pm 25 kb. **(b)** Alternate promoter usage in EWS patient samples with and
1075 without *TP53* mutations were incorporated in a Cox proportional hazards model, highlighting the
1076 potential prognostic value of the isoforms identified by M2A.

1077

1078 **Additional Files**

1079 **Additional file 1 (file type .PDF, 7 MB):**

1080 **Figure S1. NBL sample H3K27ac promoter distribution.**

1081 A comparison of promoter H3K27ac enrichment in *MYCN* amplified (MNA) NBL cell line and O-
1082 PDX samples shows a clear bimodal distribution, delineating “active” and “non-active”
1083 promoters.

1084

1085 **Figure S2. DNAm input feature pattern analysis.**

1086 The DNAm features show promoter-status-specific patterns between active, poised, and
1087 inactive promoters, emphasizing the utility of positional-based relationships in a windowed
1088 DNAm feature approach. For both 250 bp and 2,500 bp window sizes, the average scaled input
1089 feature was plotted in relationship to the TSS (ribbons represent the 95% confidence interval),
1090 stratified by the promoter status. Promoter status was determined by class occupancy of both
1091 H3K27ac and H3K4me3, either “active” or “inactive”, where (H3K27ac=active),
1092 (H3K27ac=inactive, H3K4me3=active), and (H3K27ac=inactive, H3K4me3=inactive), represents
1093 active, poised, and inactive promoters, respectively.

1094

1095 **Figure S3. Feature performance comparison: Input features vs CNN mapped features.**

1096 Using all samples included in training the vanilla M2A model (NBL, N=6), the individual feature
1097 performance (as determined by Pearson's R^2 between the feature and the response variable,
1098 H3K27ac) for each feature was plotted, comparing the distribution of performances between raw
1099 input training feature and the CNN mapped features at a particular window size (250 bp or
1100 2,500 bp). The best feature from this analysis for each window size and feature type (input or
1101 CNN mapped) was used to determine Pearson's R^2 with H3K27ac from each sample in the NBL
1102 validation set (N=10).

1103

1104 **Figure S4. M2A prediction generalizability analysis.**

1105 **(a)** A comparison between performance of the M2A model (R^2 of observed H3K27ac promoter
1106 levels and predicted levels in the test sample) with the surrogate model (represented by the
1107 highest R^2 of observed H3K27ac promoter levels in the test sample and the observed H3K27ac
1108 promoter levels in any training sample). M2A extracts generalizable features capable of out-
1109 performing the surrogate model in both the NBL validation set and the RMS test set, further

1110 highlighted in **(b)**, a comparison of surrogate model and M2A model performance using
1111 promoters from DE genes between NBL and RMS.

1112

1113 **Figure S5. M2A with transfer learning outperforms a vanilla M2A model of the same**
1114 **cancer type.**

1115 An M2A model with transfer learning (initially trained with six NBL O-PDX samples and then
1116 transferred with a single RMS sample) consistently outperforms an M2A model trained with a
1117 single RMS sample.

1118

1119 **Figure S6. Signal-to-noise analysis of ENCODE and NBL datasets.**

1120 Comparison at the observed H3K27ac promoter level **(a)** and the H3K4me3 **(b)** promoter levels
1121 revealed different signal-to-noise profiles between the ENCODE dataset and the NBL datasets,
1122 which results in a highly correlated prediction with larger RMSE values.

1123

1124 **Figure S7. M2A ENCODE cohort performance.**

1125 The distribution of M2A prediction performance (R^2), shows that M2A accurately infers both
1126 H3K27ac and H4K4me3 promoter levels in the publicly available ENCODE dataset.

1127

1128 **Figure S8. Analysis of outlier H1-ESC.**

1129 **(a)** When inferring H3K27ac promoter levels, M2A was substantially less accurate in the
1130 ENCODE sample H1-ESC, which is an outlier in the ENCODE cohort. **(b, c)** M2A-predicted
1131 H3K27ac promoter levels **(b)** are more consistent with, and more predictive of, H1-ESC gene
1132 expression than are the actual observed H1-ESC H3K27ac promoter levels **(c)**. **(d)** The
1133 hypomethylated region surrounding the promoters of genes *PSMA7* and *SS18L1* (often
1134 indicative of H3K27ac enrichment) showed inconsistent H3K27ac levels between H1-ESC
1135 ChIP-seq replicates from ENCODE.

1136

1137

1138 **Figure S9. Predicting gene expression in the ENCODE dataset.**

1139 **(a–i)** The indirect ability of M2A to predict gene expression (i.e., expressed vs. not expressed)
1140 on the basis of both M2A-predicted and observed H3K27ac promoter levels for each sample
1141 was determined by comparing the AUCs of the receiver operating characteristic (ROC) curves.

1142

1143 **Figure S10. Consistency of gene expression and H3K27ac promoter levels in the AML
1144 cohort.**

1145 The consistency, as determined by Pearson's R^2 , between the observed values for gene
1146 expression and the H3K27ac promoter levels is remarkably predictive of the performance M2A
1147 in predicting H3K27ac promoter levels in samples from the AML cohort.

1148

1149 **Figure S11. M2A accurately determines subtype differences between embryonal and
1150 alveolar RMS.**

1151 **(a)** The promoter activities of single-promoter, differentially expressed genes in the RMS
1152 subtypes ERMS and ARMS are accurately inferred by an M2A base model (trained with six O-
1153 PDX NBL samples). **(b)** The predictive performance of M2A is further boosted by transfer
1154 learning with one RMS sample. **(c, d)** The performance of M2A declines slightly when the model
1155 is applied to all promoters of differentially expressed genes **(c)**, but it recovers when an M2A
1156 model with transfer learning with only one RMS training sample is applied **(d)**.

1157

1158 **Figure S12. Kaplan–Meier log-rank analysis by mutation status in EWS.**

1159 The prognostic ability of **(a)** *TP53* or **(b)** *STAG2* mutation status in the EWS cohort was
1160 determined by the log-rank test and visualized using the Kaplan–Meier survival curve. The
1161 *STAG2* mutation status showed no significant difference in overall survivability, thus only *TP53*

1162 mutation status was considered when forming the univariate and multivariate Cox proportional
1163 hazards model.

1164

1165 **Figure S13. CpG distribution by window relative to the TSS.**

1166 To achieve feature input that is informative to the model, M2A window size selection was
1167 partially based on the number of CpGs captured by window size. Each analysis consists of 20
1168 windows surrounding each TSS at a particular window size, representing the theoretical CpG
1169 input to M2A for that particular resolution. Three different window configurations were
1170 considered, comprised of two window sizes: 1) 100 bp and 1,000 bp, 2) 250 bp and 2,500 bp,
1171 and 3) 500 bp and 5,000 bp. Due to NaNs in feature windows calculated with fewer than 2
1172 CpGs, the [100 bp, 1000 bp] model was removed from consideration (> 50% NaNs).

1173

1174 **Additional file 2 (file type: .XLSX, 179 KB).**

1175 **Table S1: H3K27ac active cancer consensus genes in 3 NBL cell lines, and 3 NBL O–PDX
1176 samples.**

1177 **Table S2: Baseline models vs. vanilla M2A predictive performance comparison.**

1178 **Table S3: M2A predictive performance in NBL cell line samples.**

1179 **Table S4: Observed H3K27ac and H3K4me3 ENCODE replicate consistencies.**

1180 **Table S5: M2A predictive performance in RMS O–PDX samples.**

1181 **Table S6: M2A RMS transfer model predictive performance in RMS O–PDX samples.**

1182 **Table S7: M2A predictive performance in ENCODE dataset.**

1183 **Table S8: M2A predictive performance in AML samples.**

1184 **Table S9: ERMS vs. ARMS DMRs and associated genes (overexpressed in ERMS).**

1185 **Table S10: ERMS vs. ARMS DMRs and associated genes (overexpressed in ARMS).**

1186 **Table S11: M2A alternate promoter usage predictive performance between ARMS and**

1187 **ERMS samples.**

1188 **Table S12: M2A predictive performance in EWS samples, before and after transfer.**

1189 **Table S13: A univariate survival analysis of differential H3K27ac promoter activity**

1190 **between TP53 mutant and TP53 wild-type EWS tumors.**

1191 **Table S14: A univariate survival analysis of alternate promoter usage between TP53**

1192 **mutant and TP53 wild-type EWS tumors.**

1193 **Table S15: ENCODE H3K27ac replicate consistency with gene expression.**

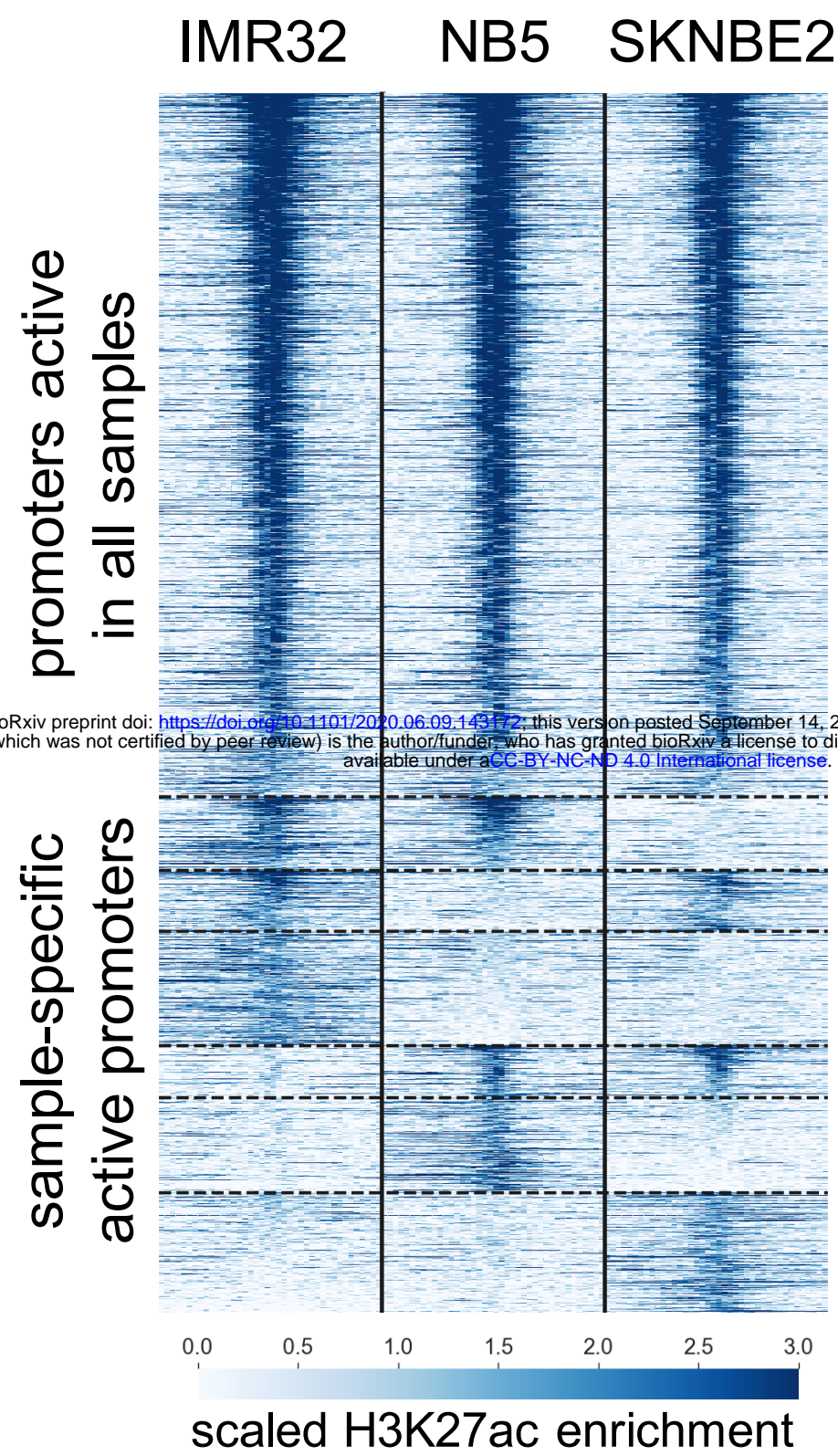
1194 **Table S16: Dataset availability.**

1195 **Table S17: M2A model topologies.**

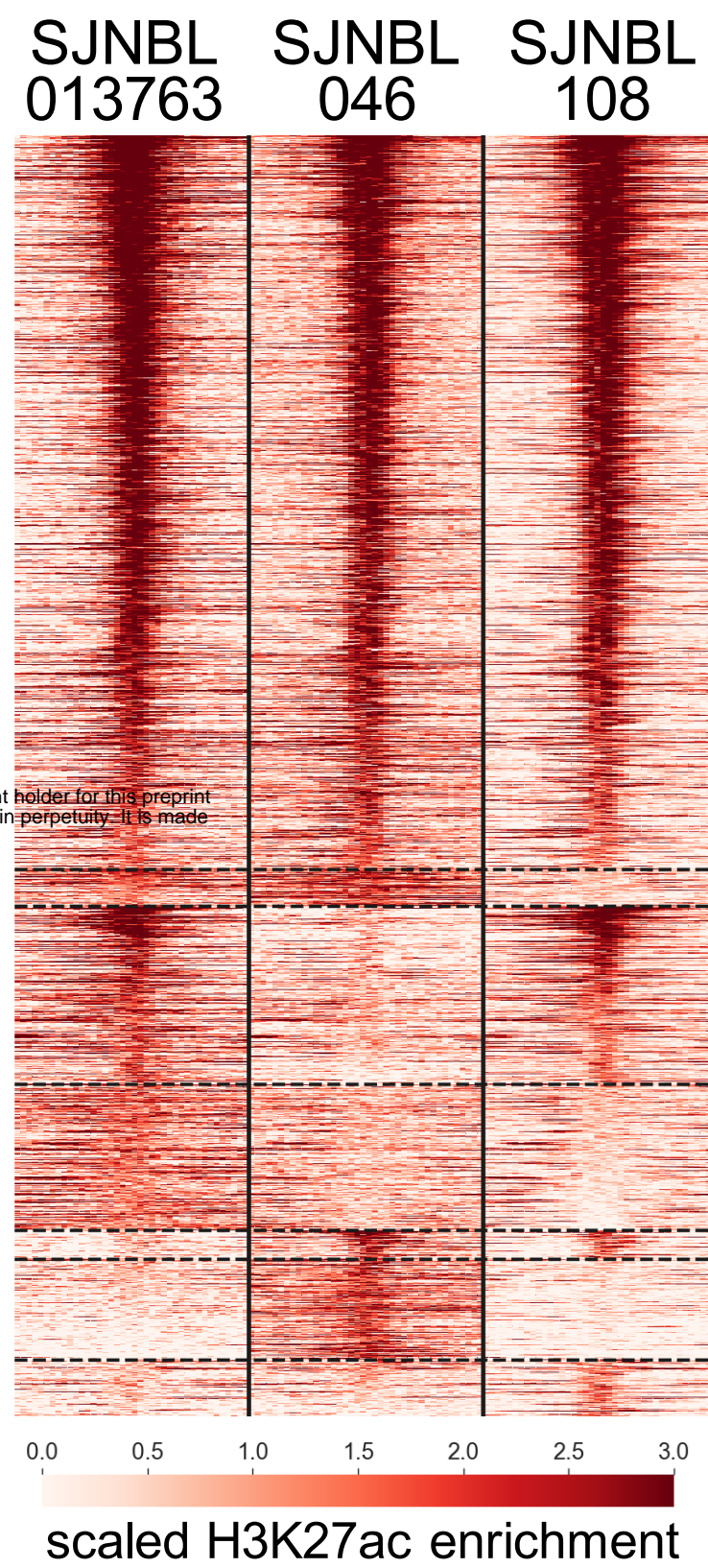
1196 **Table S18: Parameter tuning: mean performance in the NBL validation set (R^2)**

1197 **Table S19: Sample summary information.**

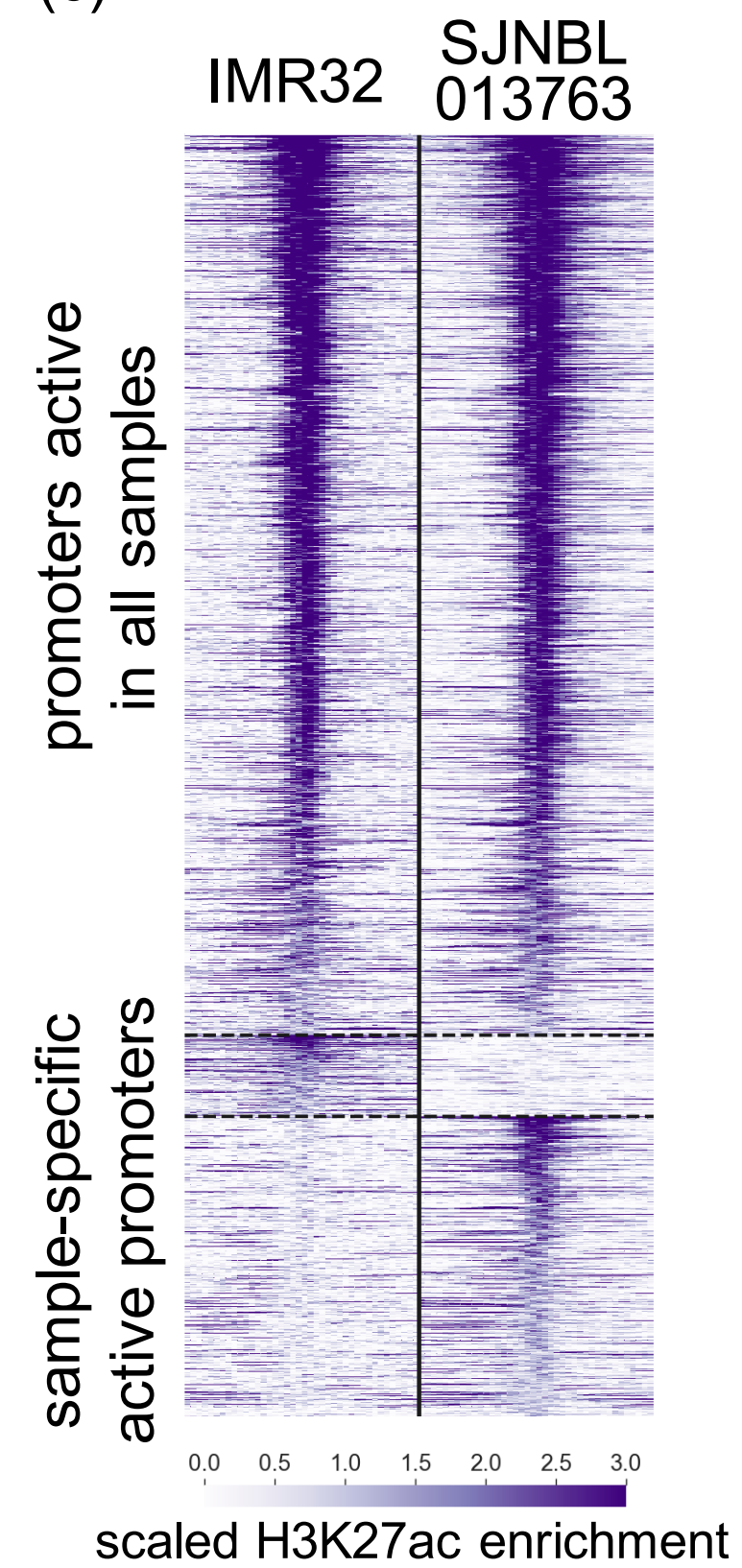
(a)



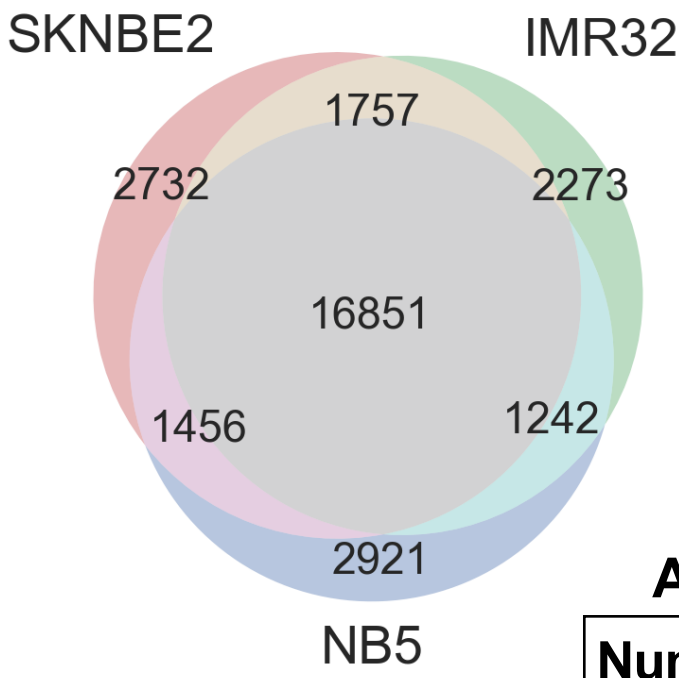
(b)



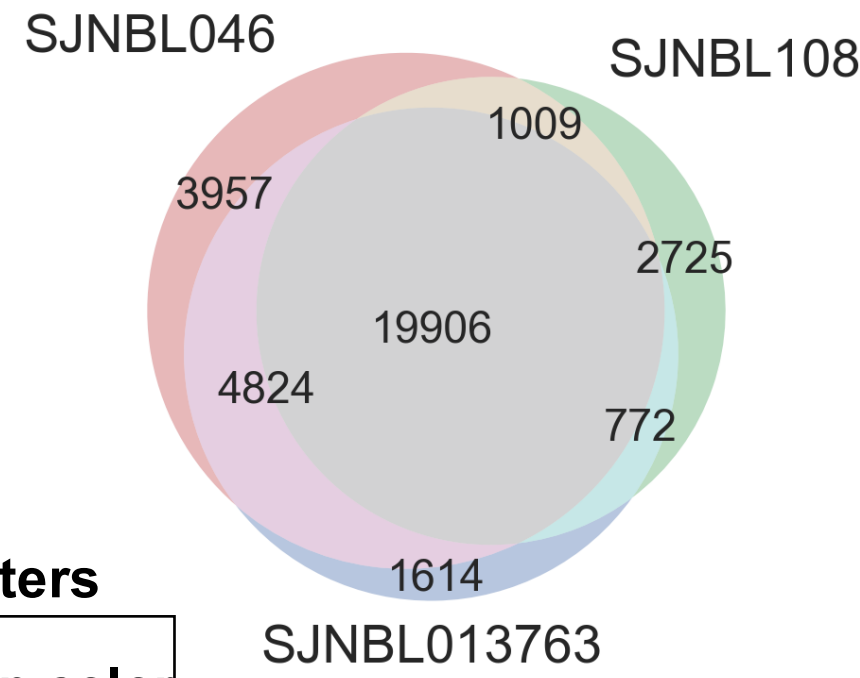
(c)



(d)

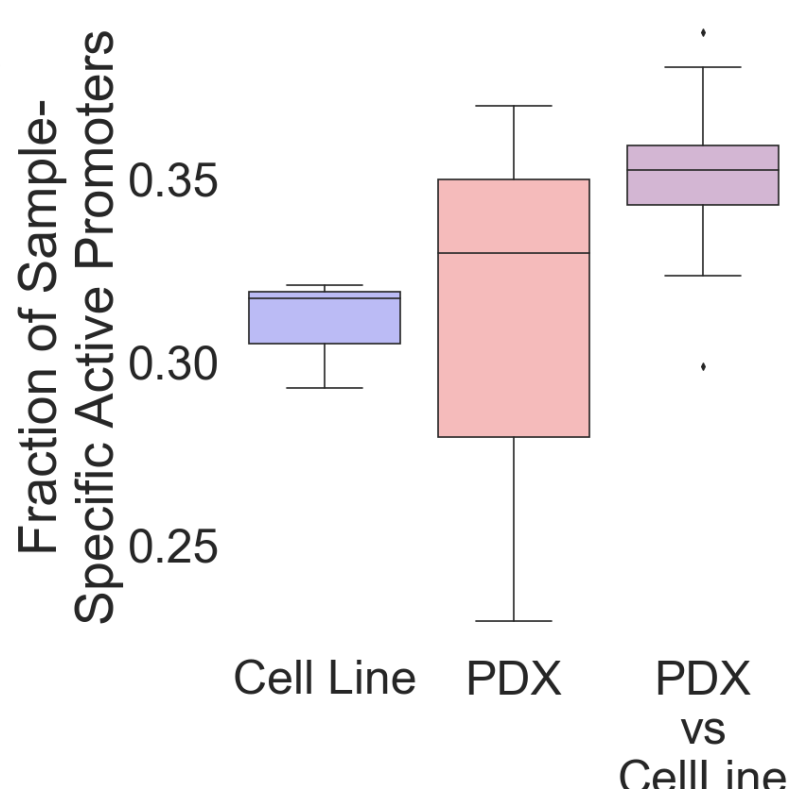


(e)

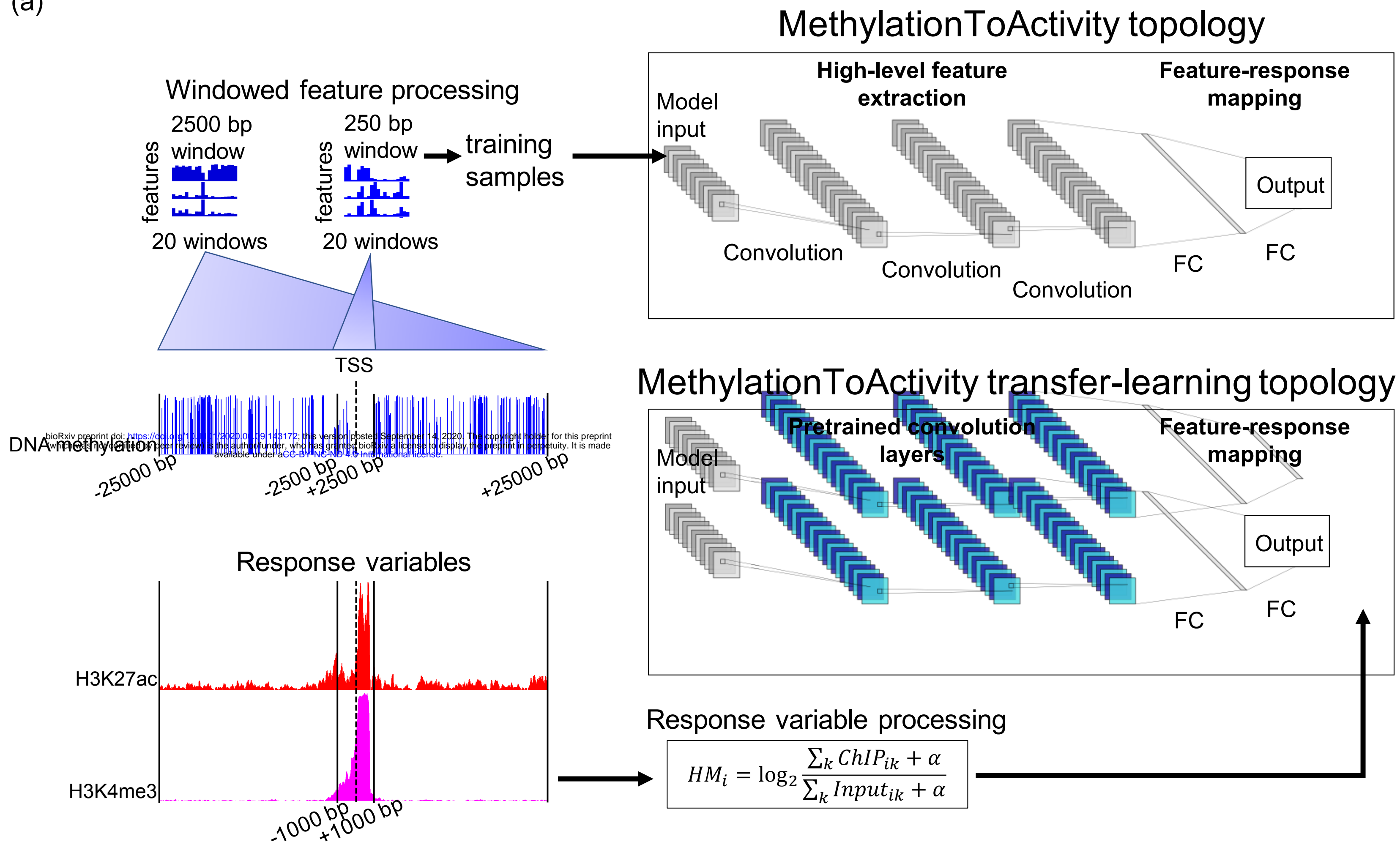


Number of samples	Group color
1 sample	
2 samples	
3 samples	

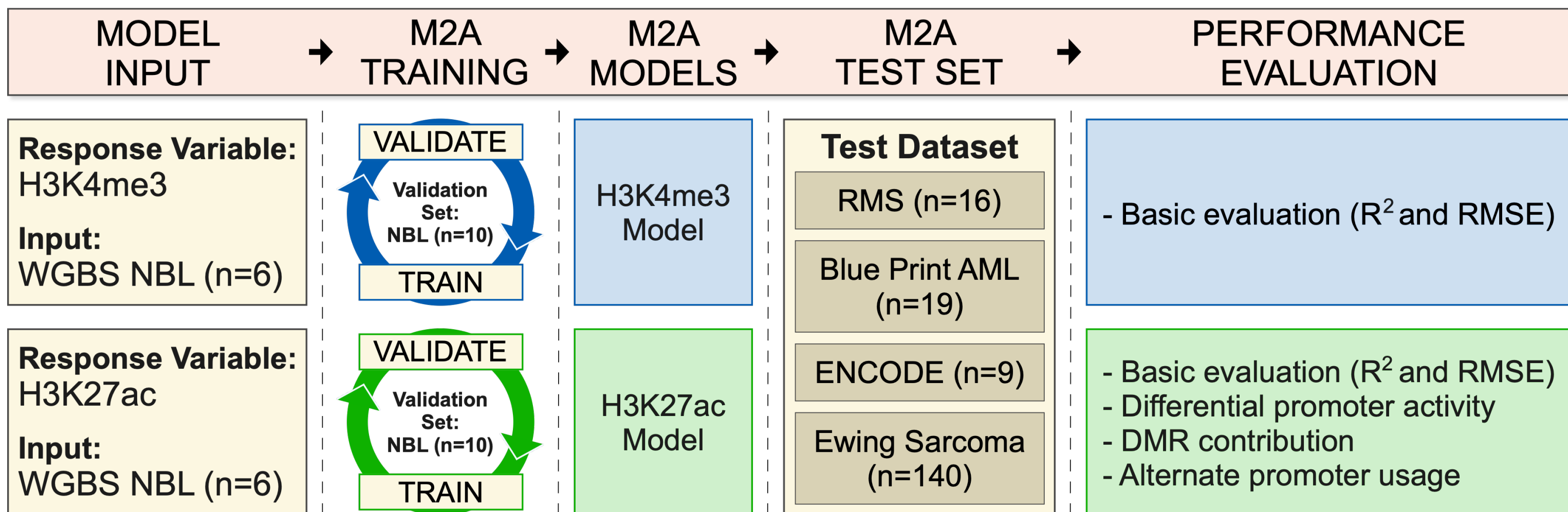
(f)



(a)

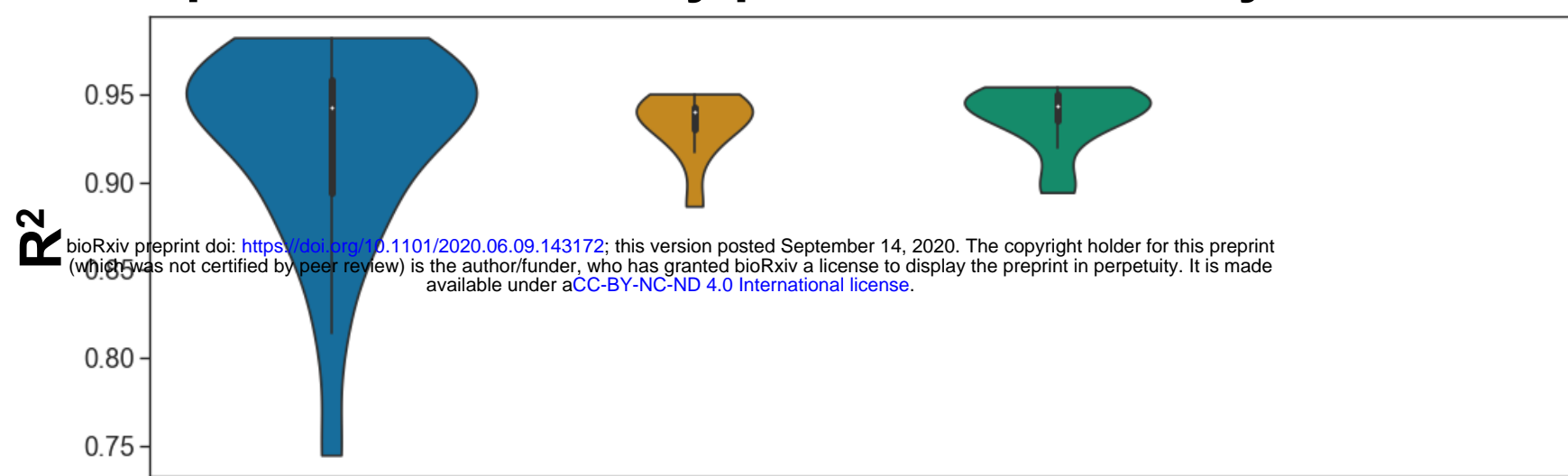


(b)



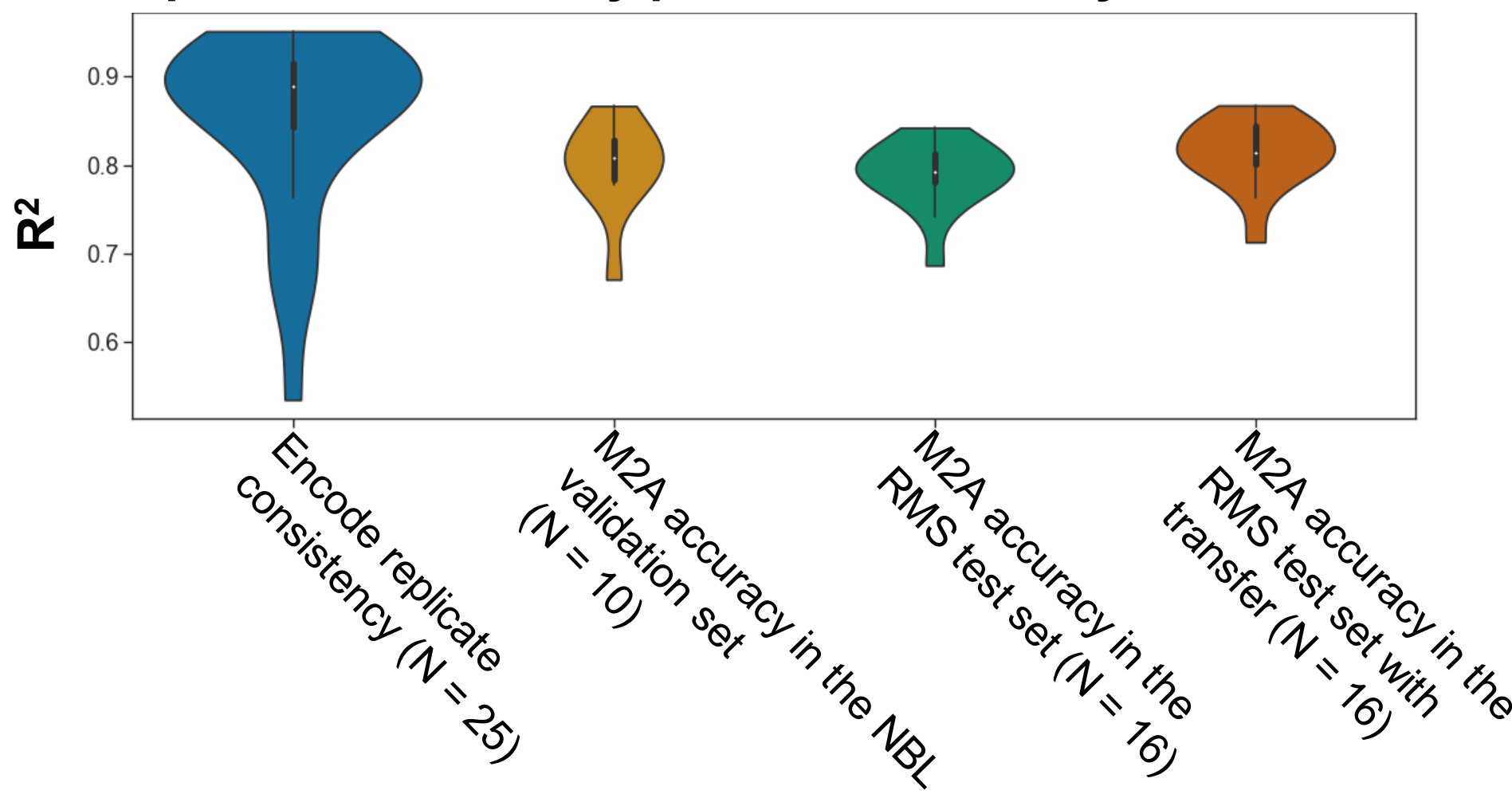
(a)

Replicate consistency/predictive accuracy for H3K4me3

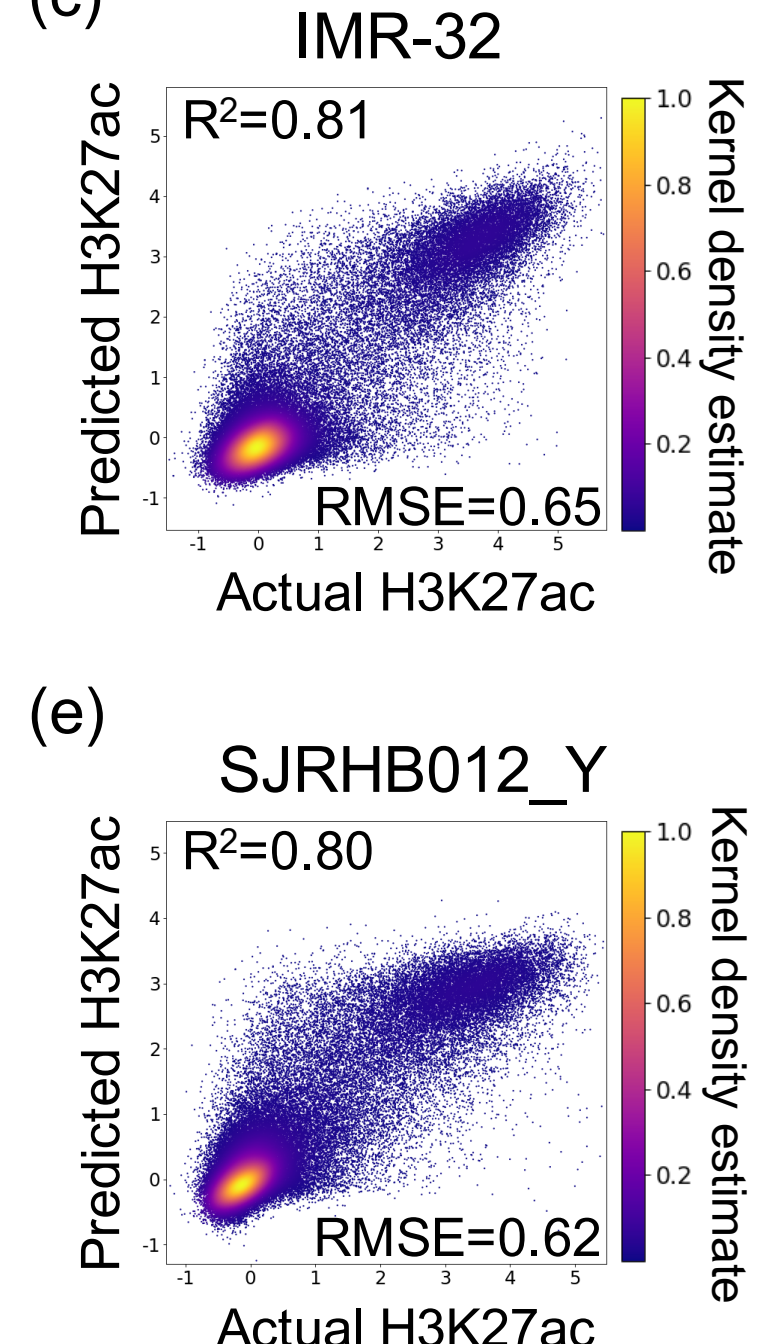


(b)

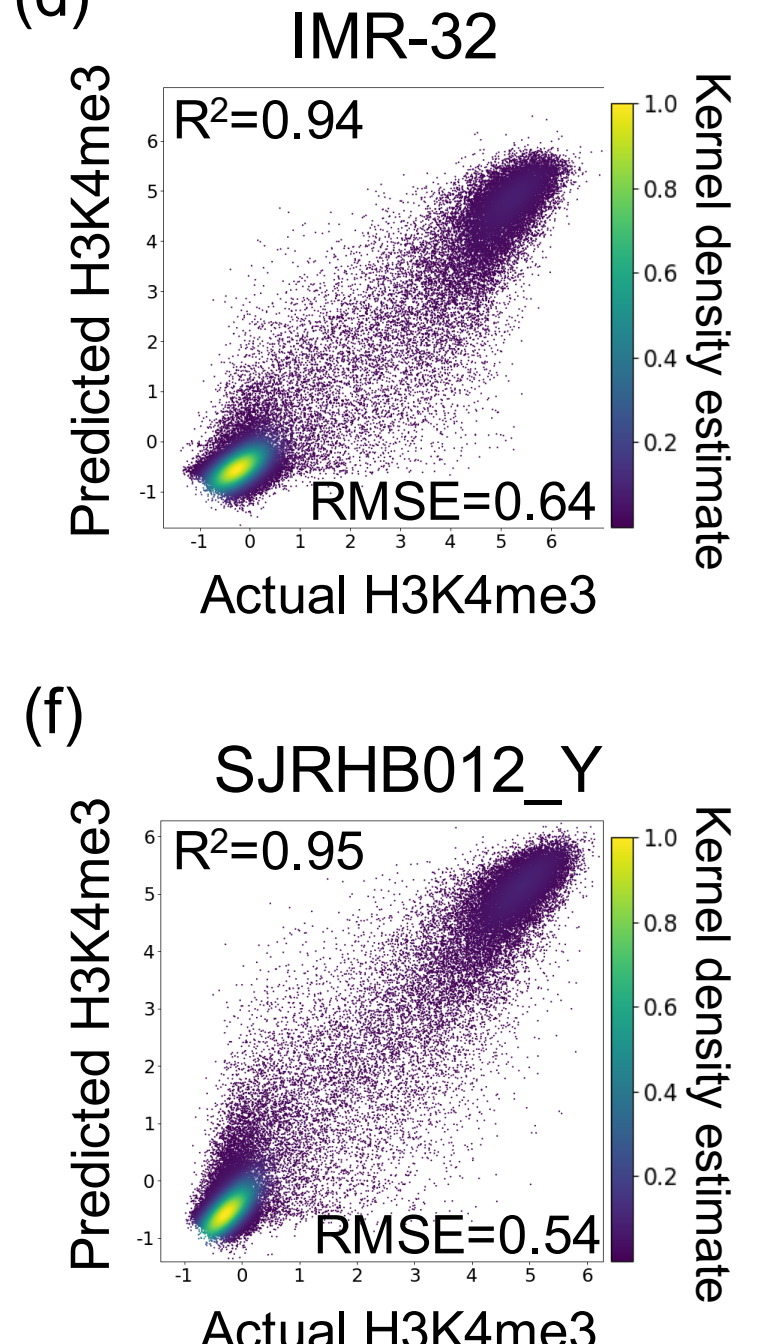
Replicate consistency/predictive accuracy for H3K27ac



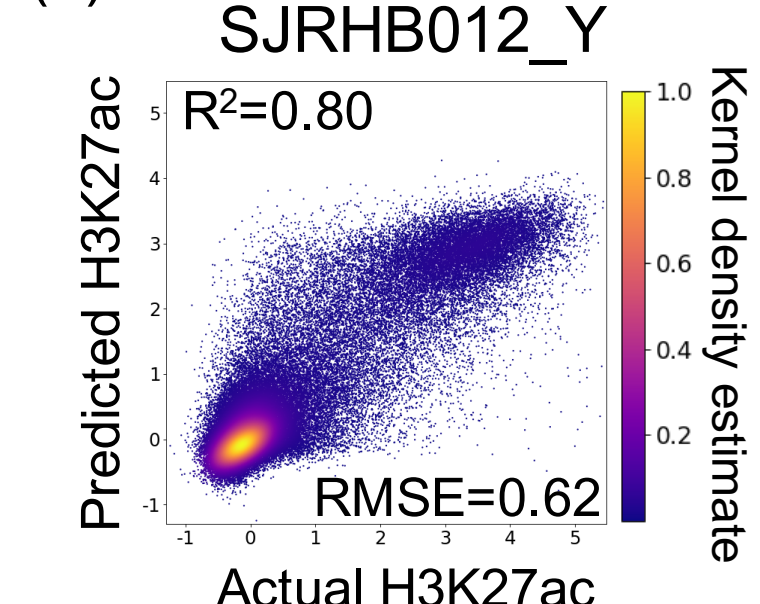
(c)



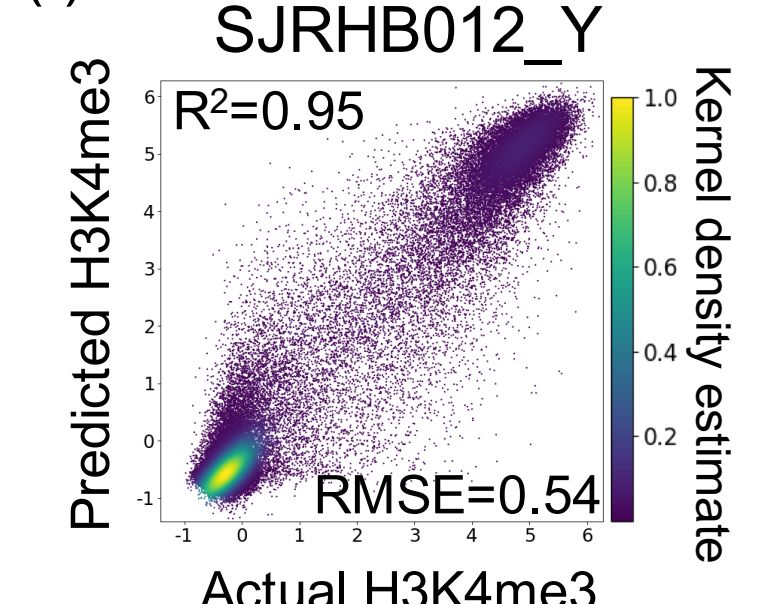
(d)



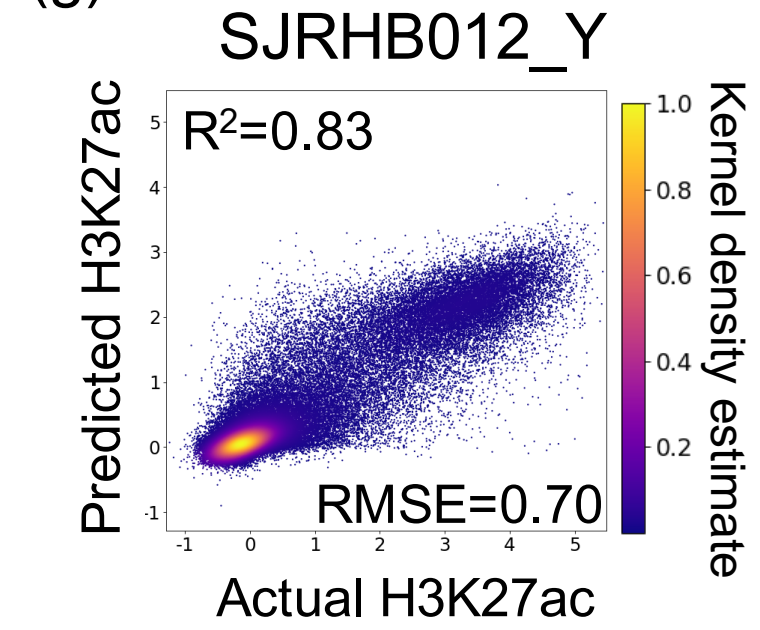
(e)



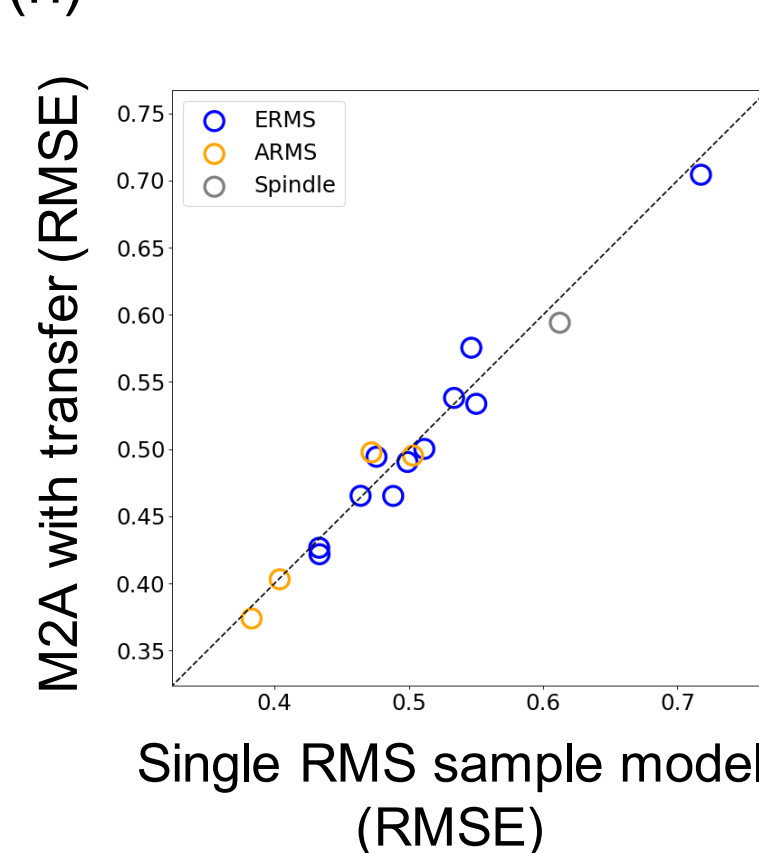
(f)



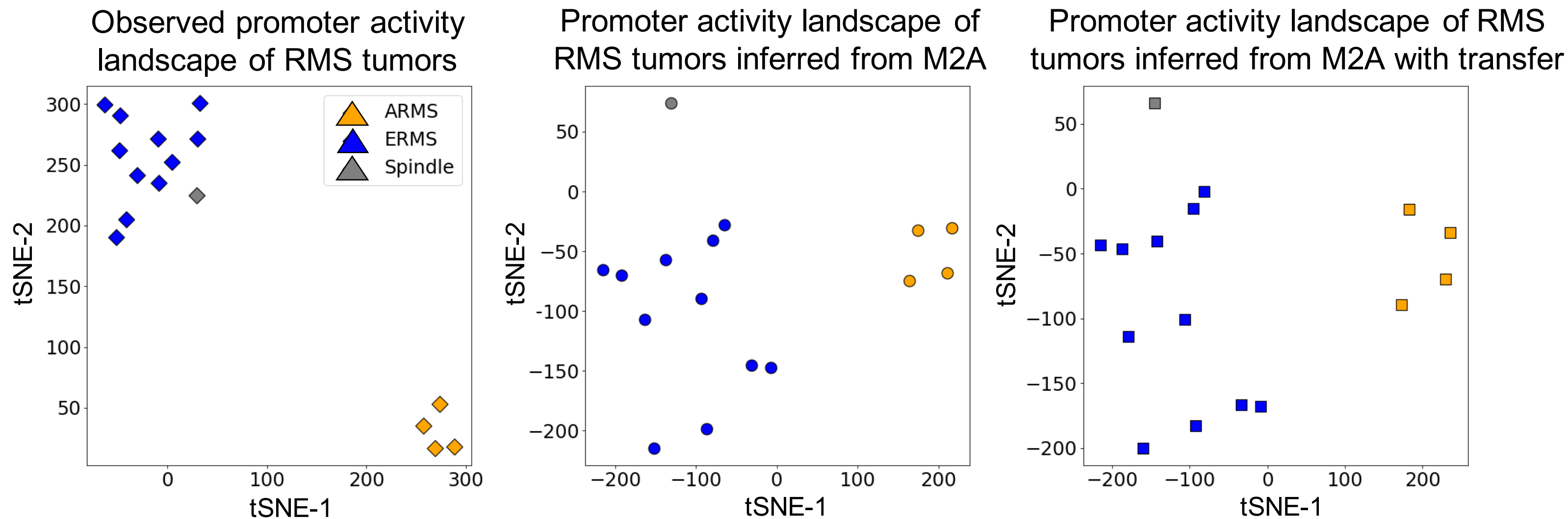
(g)



(h)

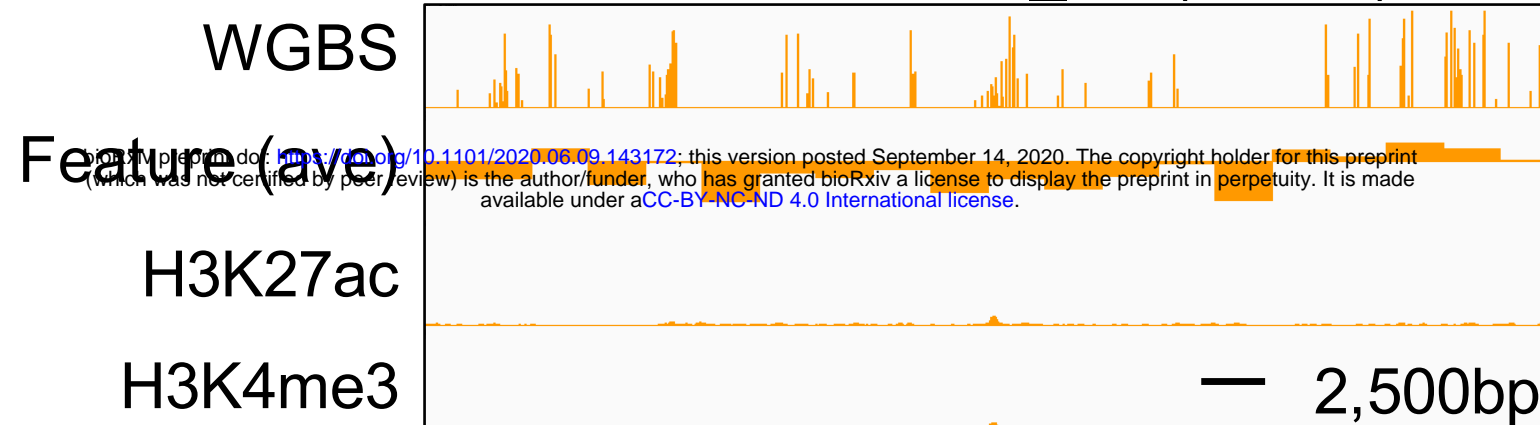


(a)



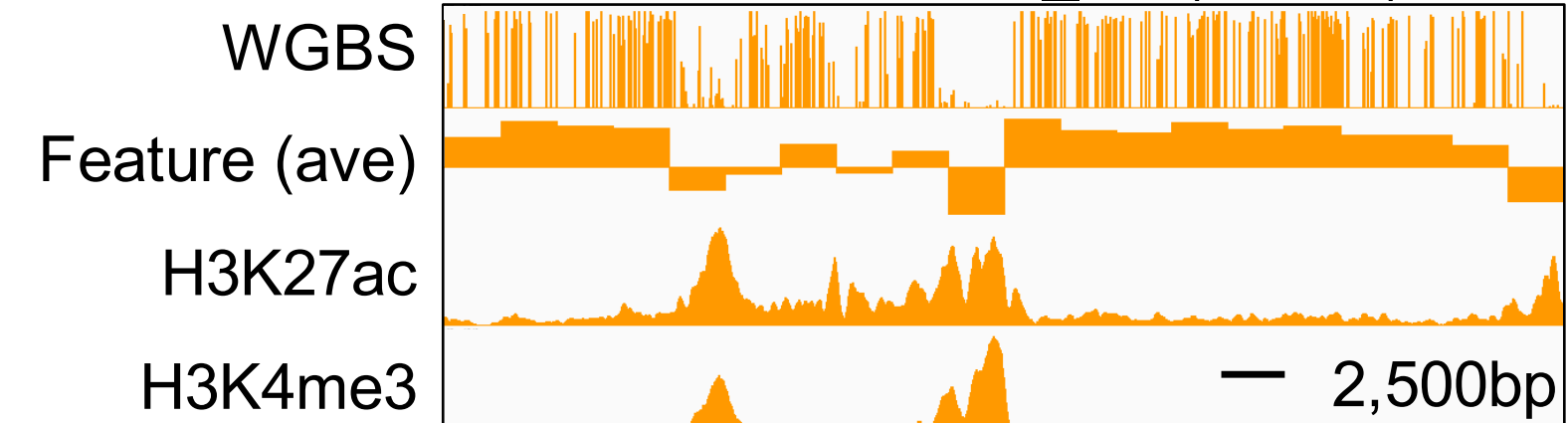
(b)

SJRHB013757_X1 (ARMS)

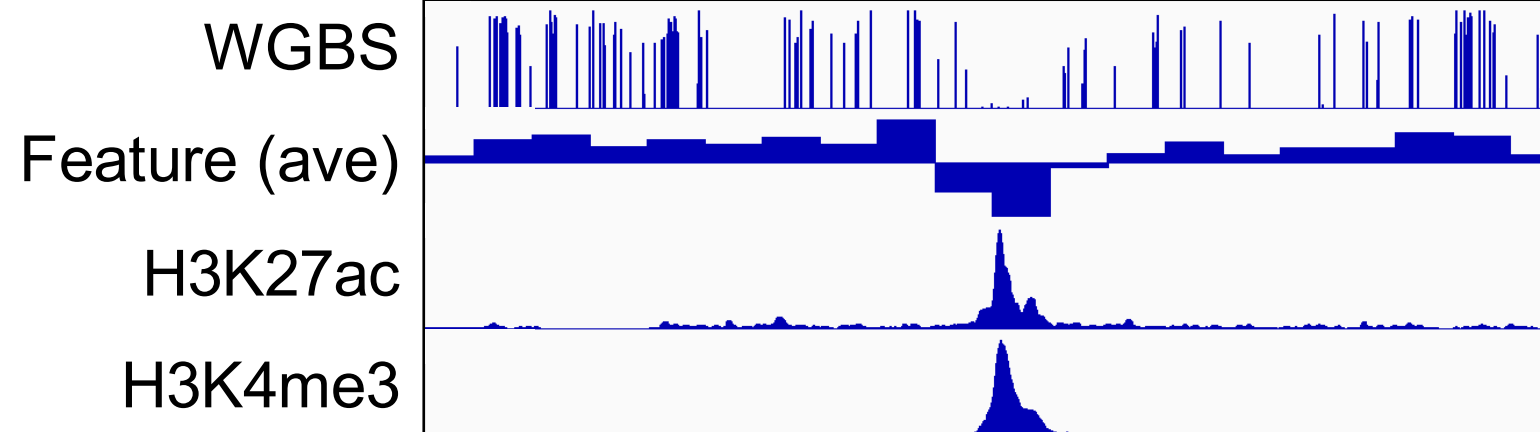


(c)

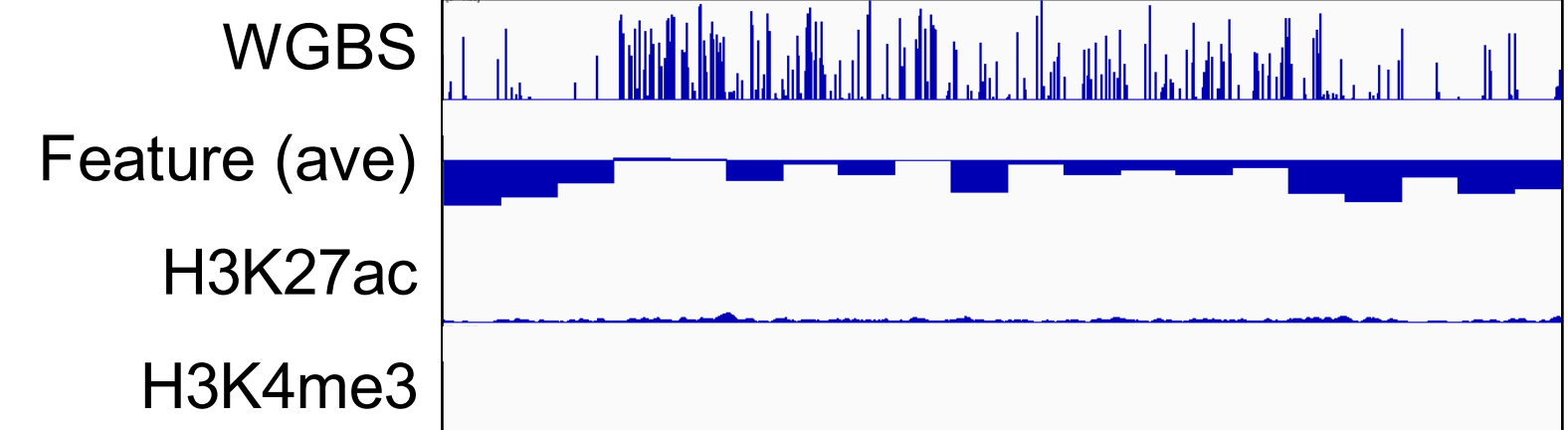
SJRHB013757_X1 (ARMS)



SJRHB013758_X2 (ERMS)

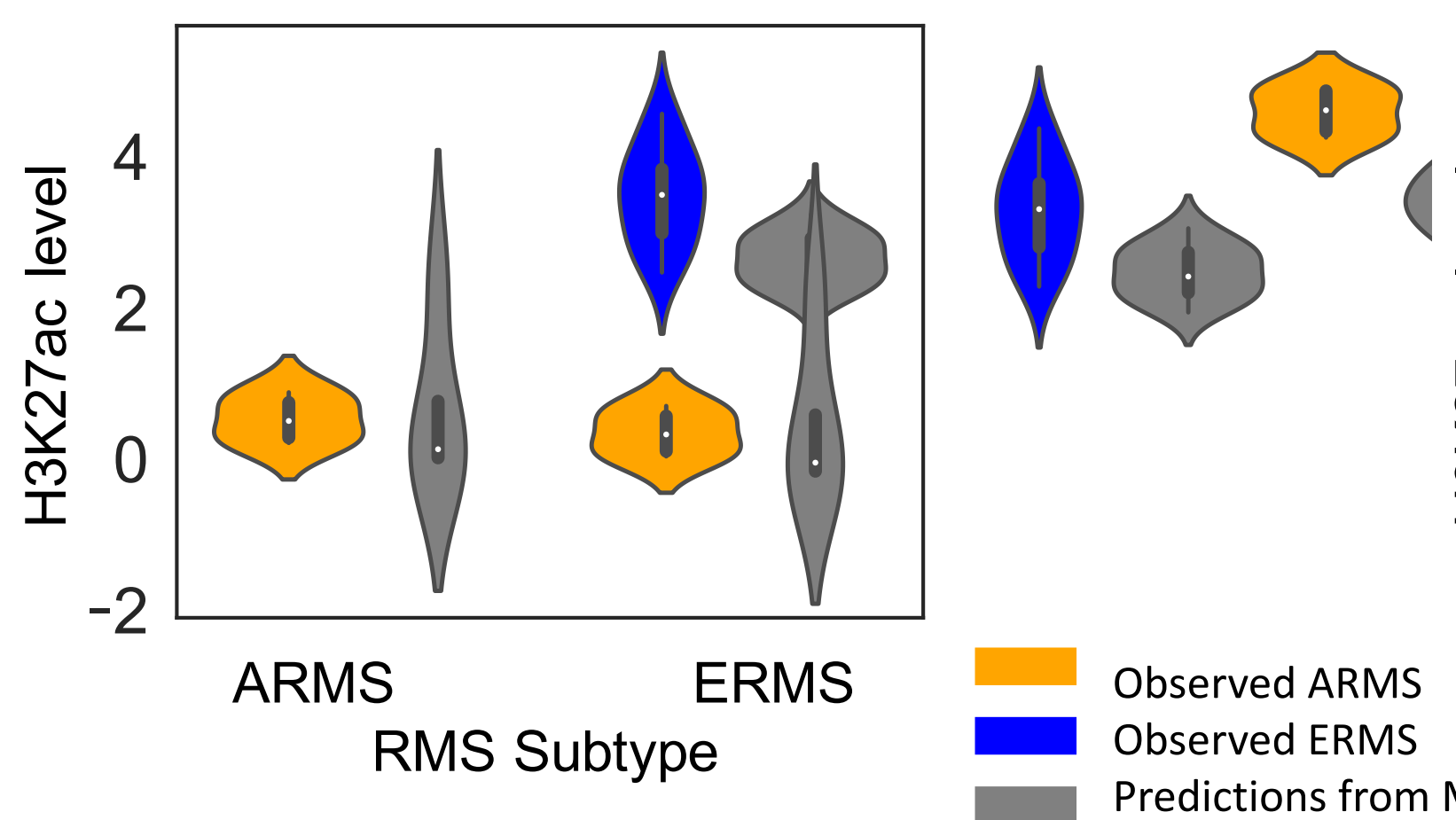


SJRHB013758_X2 (ERMS)



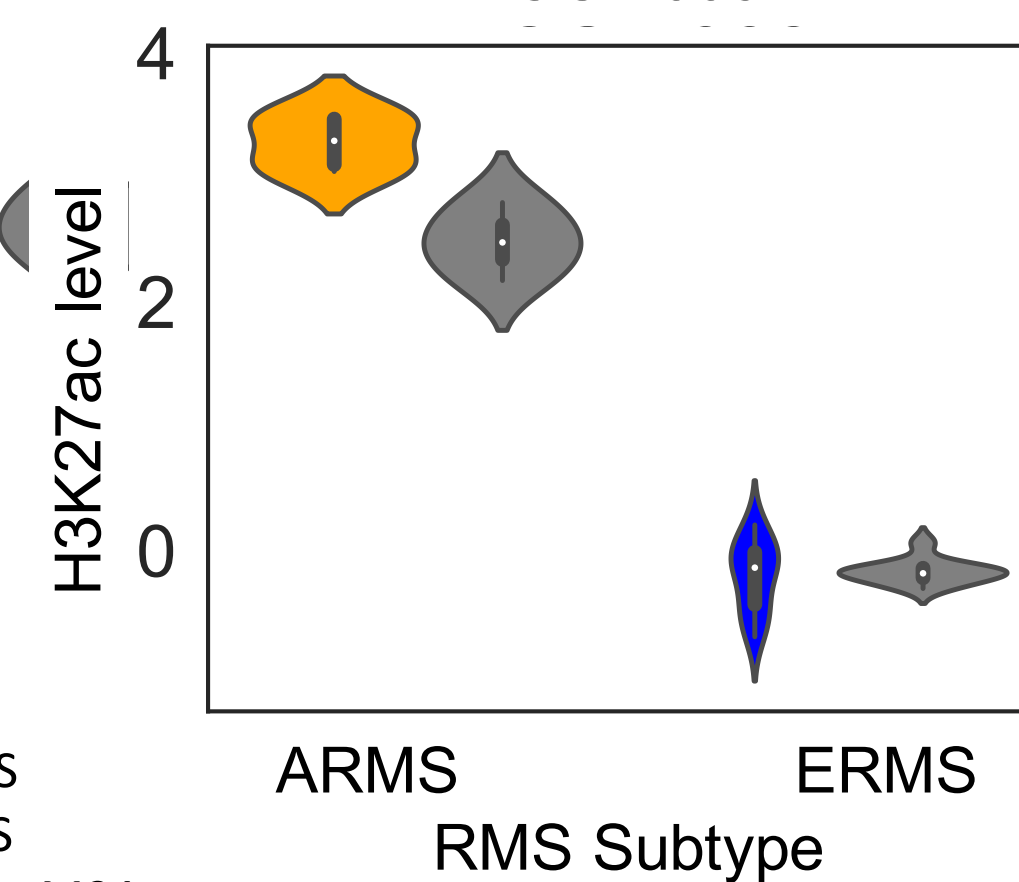
(d)

GAS2

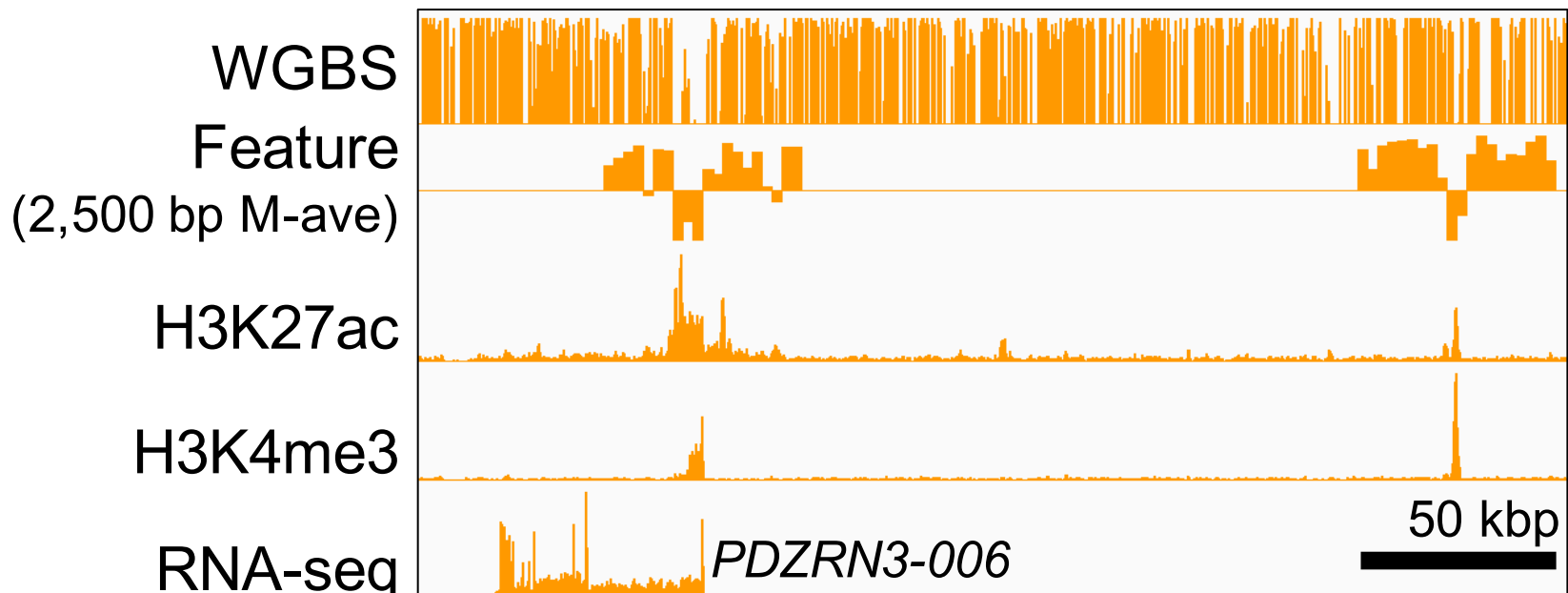


(e)

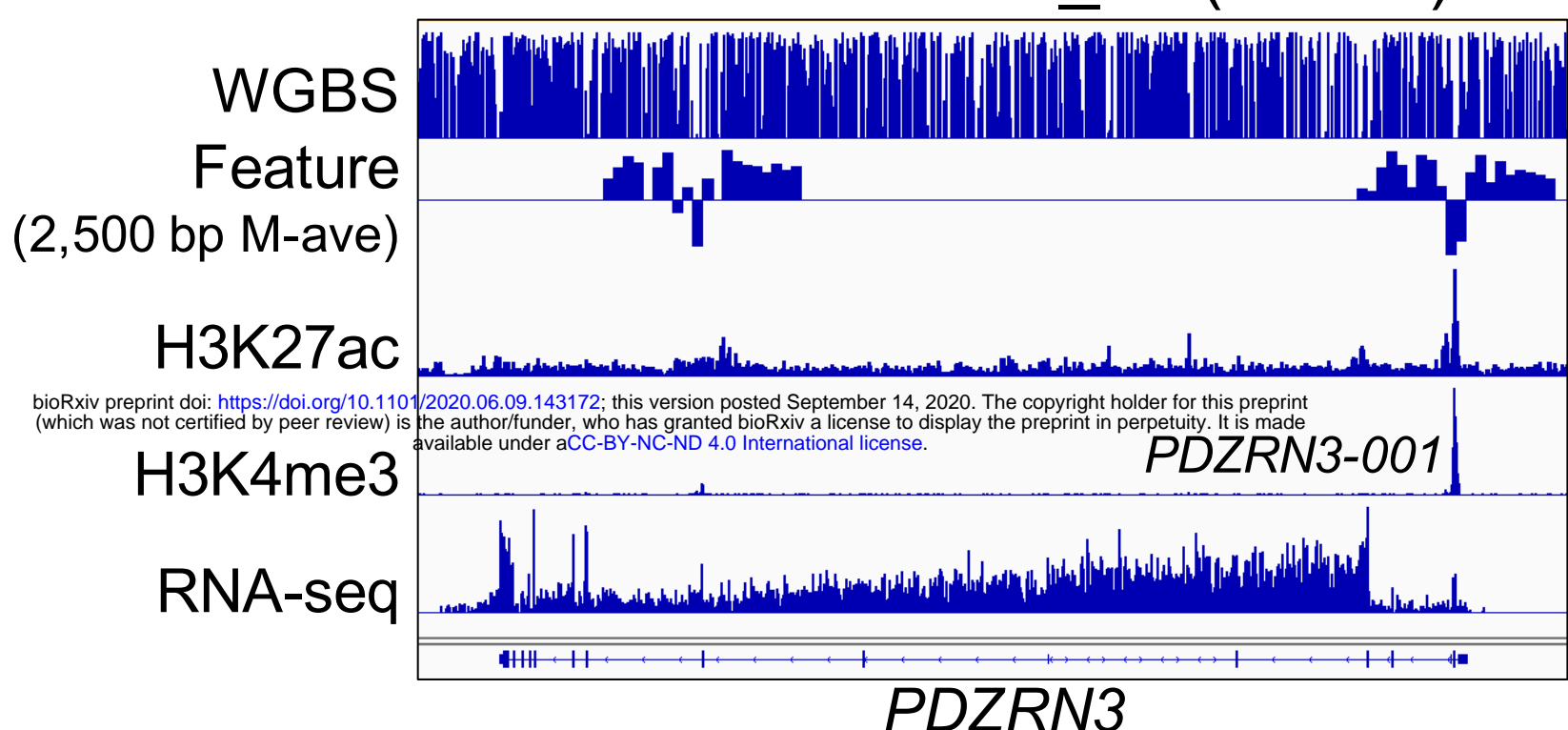
NOS1-005



(a) SJRHB010468_X1 (ARMS)



SJRHB000026_X1 (ERMS)



(b)

hazard ratio

p-value

TP53 mutation

3.01
(1.03 – 8.80)

0.044*

TNS1
(ENST00000446903.1)

0.43
(0.24 – 0.77)

0.004 **

RET
(ENST00000479913.1)

0.56
(0.30 – 1.05)

0.073

SLC27A6
(ENST00000508645.1)

1.72
(1.05 – 2.81)

0.031 *

0.2 0.5 1 2 5 10

N=72; #Events: 31; Global p-value (Log-Rank): 1.0375e-05

AIC: 211.96; Concordance Index: 0.77